Advancing Advancing Advancery and Geophysics

Downloaded from https://academic.oup.com/mnras/article/509/2/3015/6420259 by University of Connecticut user on 08 June 2022

MNRAS **509**, 3015–3042 (2022) Advance Access publication 2021 November 3

Supermassive black holes in cosmological simulations – II: the AGN population and predictions for upcoming X-ray missions

Mélanie Habouzit, ^{1,2} Rachel S. Somerville, ^{3,4} Yuan Li, ⁵ Shy Genel, ^{3,6} James Aird ¹⁰, ^{7,8} Daniel Anglés-Alcázar, ^{3,9} Romeel Davé ¹⁰, ⁷ Iskren Y. Georgiev, ¹ Stuart McAlpine ¹⁰, ¹⁰ Yetli Rosas-Guevara ¹⁰, ¹¹ Yohan Dubois, ¹² Dylan Nelson ¹⁰, ² Eduardo Banados ¹⁰, ¹ Lars Hernquist, ¹³ Sébastien Peirani ^{12,14} and Mark Vogelsberger ¹⁰15

Accepted 2021 October 22. Received 2021 October 20; in original form 2021 May 7

ABSTRACT

In large-scale hydrodynamical cosmological simulations, the fate of massive galaxies is mainly dictated by the modelling of feedback from active galactic nuclei (AGNs). The amount of energy released by AGN feedback is proportional to the mass that has been accreted on to the black holes (BHs), but the exact subgrid modelling of AGN feedback differs in all simulations. While modern simulations reliably produce populations of quiescent massive galaxies at $z \le 2$, it is also crucial to assess the similarities and differences of the responsible AGN populations. Here, we compare the AGN populations of the Illustris, TNG100, TNG300, Horizon-AGN, EAGLE, and SIMBA simulations. The AGN luminosity function (LF) varies significantly between simulations. Although in agreement with current observational constraints at z = 0, at higher redshift the agreement of the LFs deteriorates with most simulations producing too many AGNs of $L_{x,2-10\,\text{keV}} \sim 10^{43-44}\,\text{erg s}^{-1}$. AGN feedback in some simulations prevents the existence of any bright AGN with $L_{x,2-10\,\text{keV}} \geqslant 10^{45}\,\text{erg s}^{-1}$ (although this is sensitive to AGN variability), and leads to smaller fractions of AGN in massive galaxies than in the observations at $z \le 2$. We find that all the simulations fail at producing a number density of AGN in good agreement with observational constraints for both luminous ($L_{x,2-10\,\text{keV}} \sim 10^{43-45}\,\text{erg s}^{-1}$) and fainter ($L_{x,2-10\,\text{keV}} \sim 10^{42-43}\,\text{erg s}^{-1}$) AGNs and at both low and high redshifts. These differences can aid us in improving future BH and galaxy subgrid modelling in simulations. Upcoming X-ray missions (e.g. Athena, AXIS, and LynX) will bring faint AGNs to light and new powerful constraints. After accounting for AGN obscuration, we find that the predicted number density of detectable AGNs in future surveys spans at least one order of magnitude across the simulations, at any redshift.

Key words: black hole physics – methods: numerical – galaxies: evolution – galaxies: formation.

1 INTRODUCTION

In the local Universe, we observe supermassive black holes (BHs) with masses in the range $M_{\rm BH} = 4 \times 10^4 - 10^{10} \, \rm M_{\odot}$ in galaxies of different types (star-forming, quiescent galaxies), and from dwarf to large elliptical galaxies (Greene, Strader & Ho 2019). BHs are ubiquitous in our Universe, and are believed to play a crucial role

in the evolution of galaxies through their energetic feedback (Silk & Mamon 2012; Somerville & Davé 2015, and references therein). Evidence for the co-evolution between BHs and their host galaxies can be found in empirical relationships between BH mass and e.g. galaxy total stellar mass, bulge mass, and velocity dispersion (e.g. Magorrian et al. 1998; Häring & Rix 2004; Gültekin et al. 2009). Beyond the local Universe, we have no choice but to observe only a fraction of the BH population: the active and accreting BHs, i.e. the active galactic nuclei (AGNs), which are the focus of this paper.

¹Max-Planck-Institut für Astronomie, Königstuhl 17, D-69117 Heidelberg, Germany

²Zentrum für Astronomie der Universität Heidelberg, ITA, Albert-Ueberle-Str 2, D-69120 Heidelberg, Germany

³Center for Computational Astrophysics, Flatiron Institute, New York, NY 10010, USA

⁴Department of Physics and Astronomy, Rutgers University, 136 Frelinghuysen Road, Piscataway, NY 08854, USA

⁵Department of Physics, University of North Texas, Denton, TX 76203, USA

⁶Columbia Astrophysics Laboratory, Columbia University, 550 West 120th Street, New York, NY 10027, USA

⁷Institute for Astronomy, Royal Observatory, University of Edinburgh, Edinburgh EH9 3HJ, UK

⁸School of Physics and Astronomy, University of Leicester, University Road, Leicester LE1 7RJ, UK

Department of Physics, University of Connecticut, 196 Auditorium Road, U-3046, Storrs, CT 06269-3046, USA

¹⁰Department of Physics, University of Helsinki, Gustaf Hällströmin katu 2a, PO Box 64, FI-00014 Helsinki, Finland

¹¹Donostia International Physics Centre (DIPC), Paseo Manuel de Lardizabal 4, E-20018 Donostia-San Sebastian, Spain

¹²Institut d'Astrophysique de Paris, Sorbonne Universités, CNRS, UMR 7095, 98 bis bd Arago, F-75014 Paris, France

¹³Harvard–Smithsonian Center for Astrophysics, 60 Garden Street, Cambridge, MA 02138, USA

¹⁴Observatoire de la Côte d'Azur, Laboratoire Lagrange, Université Côte d'Azur, Boulevard de l'Observatoire, CS, F-34229 Nice, France

¹⁵Department of Physics, Kavli Institute for Astrophysics and Space Research, MIT, Cambridge, MA 02139, USA

^{*} E-mail: habouzit@iap.fr

Hydrodynamical cosmological simulations, such as Illustris, TNG100, Horizon-AGN, EAGLE, and SIMBA (Vogelsberger et al. 2013, 2014b, 2020; Dubois et al. 2014, 2016; Genel et al. 2014; Crain et al. 2015; Schaye et al. 2015; Sijacki et al. 2015; McAlpine et al. 2016; Volonteri et al. 2016; Nelson et al. 2018; Davé et al. 2019; Thomas et al. 2019), are a great tool to study the properties of the AGN population and its connection to the full BH population. BHs are modelled as collisionless sink particles, each of them being able to accrete surrounding gas, merge with other BH sink particles (often immediately after galaxy mergers), and to release energy into the neighbouring gas cell/particle elements. The latter process is called AGN feedback, and is thought to be able to shape the massive end of the galaxy mass function (e.g. Silk & Mamon 2012). In these simulations, we can follow the accretion rates on to the BHs, and therefore, assess the luminosity of the BHs by assuming that a given fraction of the accreted mass is converted to light and radiated away. The radiative efficiency typically ranges from 10 to 20 per cent in the simulations, and is often used to calibrate the efficiency of AGN feedback and reproduce the empirical $M_{\rm BH}$ - M_{\star} scaling relations. Large-scale simulations with ~ 100 cMpc side length unfortunately do not have sufficient resolution to resolve the small scales needed to physically capture the physics of the AGN accretion disc (Negri & Volonteri 2017; Angles-Alcazar et al. 2020, and references therein). Nevertheless, it is possible to estimate an accretion rate following the Bondi-Hoyle accretion model (Bondi & Hoyle 1944), which describes the spherical stationary inflow of a perfect, non-viscous, non-self-gravitating gas on to a BH. In practice, we assume in most of these simulations that the accretion rate is proportional to $M_{\rm BH}^2$ and is related to the properties of the surrounding gas. One exception is the SIMBA simulation that employs a gravitational torque accretion model (Hopkins & Quataert 2011; Anglés-Alcázar et al. 2017a), in which the accretion rate is almost independent of BH mass. Largescale simulations produce a large number of galaxies with stellar mass in the range $M_{\star} = 10^9 - 10^{13} \,\mathrm{M}_{\odot}$. They allow us to understand the population of AGNs in diverse environments and in a broad galaxy mass range. However, simulations also carry a lot of uncertainties through their subgrid modelling. Looking in detail at the active BHs can provide us with additional channels to constrain the subgrid physics of the simulations. It is important to notice that large-scale cosmological simulations were not calibrated to reproduce any of the AGN properties, which are thus true predictions from the simulations.

Observationally, the AGN luminosity function constrains a combination of BH quantities: the BH mass distribution and the accretion rate, or the Eddington ratio distributions. This provides information on the growth of BHs through cosmic times. Constraints on the luminosity function and on the number density of AGN have shown over the years that the population of AGNs strongly evolves with time. The number of AGNs reaches a peak at $z \sim 1$ –2, and declines at lower redshift. The peak of activity depends on the luminosity of the AGN, with more luminous AGNs of $L_{\rm x, 2-10 \; keV} \sim 10^{44-45} \; {\rm erg \; s^{-1}}$ having most of their activity at $z \sim 2$ and a sharp decline afterwards. Fainter AGNs with $L_{\rm x,\,2-10\;keV} < 10^{44}\,{\rm erg\,s^{-1}}$ peak at $z\sim 1$ but present a smoother decline later on compared to brighter AGNs (Ueda et al. 2014; Aird et al. 2015; Buchner et al. 2015). While they provide crucial information, the various observational constraints on the luminosity function and the number density of AGN show some differences. At $z \leq 3$, the observational discrepancies on the luminosity functions remain small and a good agreement between the results of e.g. Miyaji et al. (2015), Buchner et al. (2015), and Koulouridis et al. (2018) is found. Differences increase at higher redshift ($z \ge 4$). For example, the hard X-ray luminosity function of Georgakakis et al. (2015) has a much lower normalization at the

faint end $(L_{x,\,2-10\,\mathrm{keV}} \leqslant 10^{44}\,\mathrm{erg\,s^{-1}})$ than the functions derived by Aird et al. (2010), Ueda et al. (2014), Vito et al. (2014, 2016), and Buchner et al. (2015). For the bright end $(L_{x,\,2-10\,\mathrm{keV}} \geqslant 10^{44}\,\mathrm{erg\,s^{-1}})$, Giallongo et al. (2015) find a much lower normalization than Buchner et al. (2015), while having consistent results for the faint end. The AGN population is complex and observationally there are still differences in the shape of the faint and bright ends of the luminosity function (particularly at $z \geq 3$), and in their overall normalization.

A crucial aspect of AGN is how many of them are significantly obscured. Obscuration arises from the gas and dust both near the BHs and further away in the host galaxies (Buchner & Bauer 2017; Ramos Almeida & Ricci 2017, for the relative contributions of the small-scale versus galaxy-scale gas/dust content). Most of the obscuration is likely occurring on small scales that cannot be resolved by large-scale cosmological simulations. The fraction of heavily obscured AGNs, i.e. the Compton-thick AGNs embedded in hydrogen column densities of $N_{\rm H} \ge 10^{24} \, {\rm cm}^{-2}$, is almost entirely derived from X-ray surveys (Brandt & Alexander 2015). Optical AGN surveys are biased against even moderately obscured AGN. Mid-infrared emission is, a priori, not biased against obscuration but the emission from the galaxy component can be significant. At low redshift, many Compton-thick AGNs have been observed but at z >3 their detection becomes challenging with current X-ray telescopes. Thus far, only a few $z \ge 3$ Compton-thick AGNs have been detected, with the most distant one at z = 4.76 (Gilli et al. 2011; Vito et al. 2014, 2016; Marchesi et al. 2016). These AGNs could potentially represent 30-50 per cent or more of the AGN population (Gilli et al. 2007; Gilli, Comastri & Hasinger 2007; Merloni et al. 2014; Ueda et al. 2014). Obscuration is a key unknown of the AGN population.

Improving the knowledge of the fraction of obscured AGNs will require the use of new X-ray instruments with higher sensitivity, but also the ability to explore larger areas on the sky to gain statistics. The upcoming Athena X-ray mission (Nandra et al. 2013) and AXIS (Mushotzky 2018) and LynX (The Lynx Team 2018) concept X-ray missions will increase by at least one order of magnitude the current X-ray flux sensitivity, and aim at observing the Universe up to high redshifts to reveal fainter and fainter AGNs. These missions will follow the large number of successful X-ray surveys that have been employed in the field over the last decades (e.g. eRASS, XMM-XXL, Stripe-82X, XMM-Atlas, X-Bootes, DEEP2-F1, XMM-COSMOS, C-COSMOS, X-UDS, J1030, COSMOS Legacy, SSA 22, AEGIS-XS CDFS, and CDFN), showing that X-ray selection is powerful to understand BH growth in the distant Universe (see Brandt & Alexander 2015, for a review).

In the first paper of this series (Habouzit et al. 2020), we examined the BH population of the Illustris, TNG100, TNG300, Horizon-AGN, EAGLE, and SIMBA simulations (Vogelsberger et al. 2013, 2014b; Dubois et al. 2014, 2016; Genel et al. 2014; Crain et al. 2015; Schaye et al. 2015; Sijacki et al. 2015; McAlpine et al. 2016; Volonteri et al. 2016; Anglés-Alcázar et al. 2017a; Nelson et al. 2018; Davé et al. 2019; Thomas et al. 2019, 2020). While all being calibrated with an empirical scaling relation, the shape and normalization of the $M_{\rm BH}$ – M_{\star} mean relation and its evolution vary from one simulation to another (Habouzit et al. 2020), because these aspects are driven by the subgrid physics of both the BH and the galaxy models [e.g. seeding, supernova (SN) and AGN feedback, and BH accretion modelling]. Given this, and the difficulty of measuring $M_{\rm BH}$ and the galaxy properties in a wide range of galaxies, even in the local Universe, the $M_{\rm BH}$ - M_{\star} does not appear as the most ideal way of constraining further the BH population in cosmological simulations nowadays. Therefore, in this second paper we explore the AGN population produced by the six large-scale cosmological simulations.

We aim at providing the reader with the fundamental quantities that characterize the demographics of active BHs in cosmological simulations. We assess how different models can affect the AGN population, and show that Illustris, TNG, Horizon-AGN, EAGLE, and SIMBA all produce different populations of AGNs. These populations are in good agreement with some observational constraints, but can also show significant differences with some others. We will show that in general it appears very challenging for a given simulation to produce a population of AGNs in good agreement with observations at both high and low redshifts and for both faint and bright AGNs. We also deliver predictions on the AGN population that the Athena, AXIS, and LynX missions will be able to see. To confront our results with future observations, we apply empirically motivated models for the fraction of obscured AGNs to our initial catalogues of simulated AGNs. We show that accessing the faint regime of the AGN population could help discriminate different cosmological simulation models. While an interesting goal of these space missions is to improve our knowledge beyond z = 6, here we restrict our analysis to z < 6, a redshift range for which cosmological simulations can already be compared and constrained with current observations.

We first investigate what population of BHs powers the AGN in Section 3.1. In Section 3.2, we present the distributions of the Eddington ratios of the BH populations. We compute the AGN luminosity functions in Section 4, and the AGN number density in Section 4.2. In the following sections, we investigate which galaxies the AGNs live in. In particular, we derive the probability of galaxies to host an AGN (i.e. the galaxy occupation fraction) in Section 5 and compare it with constraints in massive galaxies. Finally, in Section 6 we synthesize the AGN population that will be detectable by the upcoming Athena mission, and the AXIS and LynX concept missions, and explore how we could use these new constraints to improve the BH/galaxy subgrid models in simulations.

2 METHODOLOGY: COSMOLOGICAL SIMULATIONS, AGN LUMINOSITY, AND OBSCURATION

2.1 Cosmological simulations

We use the six Illustris, TNG100, TNG300, Horizon-AGN, EAGLE, and SIMBA large-scale cosmological hydrodynamical simulations. These simulations model the time evolution of the dark matter and baryonic matter content in an expanding space-time. Due to the large dynamical range needed to follow the non-linear evolution of galaxies, the simulations all employ subgrid modelling for e.g. star formation, stellar and SN feedback, BH formation, evolution, and feedback. While all the same in spirit, subgrid models vary from simulation to simulation as explained in the first paper of this series (Habouzit et al. 2020). Detailed descriptions of the simulations and their BH modelling can be found in Genel et al. (2014) and Vogelsberger et al. (2014b) for Illustris, Pillepich et al. (2018) and Weinberger et al. (2018) for TNG, Dubois et al. (2016) and Volonteri et al. (2016) for Horizon-AGN, Schaye et al. (2015), Rosas-Guevara et al. (2015, 2016), and McAlpine et al. (2017, 2018) for EAGLE, and Davé et al. (2019), Thomas et al. (2019, 2020), and Anglés-Alcázar et al. (2017a) for SIMBA. These simulations were calibrated to reproduce one of the empirical scaling relations between BH mass and galaxy properties identified in the local Universe. No calibration on the properties of the active population of BHs was used.

BH particles are seeded either in massive haloes of $\geqslant 10^{10} \, \rm M_{\odot}$ or in galaxies of $M_{\star} \geqslant 10^{9.5} \, \rm M_{\odot}$, or based on the local gas properties (Dubois et al. 2016). Initial BH masses range in $M_{\rm BH} \sim 10^4 - 10^6 \, \rm M_{\odot}$.

BHs can grow by BH-BH mergers and gas accretion. Most of the simulations model BH gas accretion with the Bondi-Hoyle-Lyttleton model, or some variations of its formalism, e.g. including a magnetic field component (TNG; Pillepich et al. 2018) or a viscous disc component (EAGLE; Rosas-Guevara et al. 2015; Schaye et al. 2015). The SIMBA simulation employs a two-mode gas accretion model (the two modes can be simultaneous; Anglés-Alcázar et al. 2017a; Davé et al. 2019): gravitational torque-limited accretion model for the cold gas component ($T < 10^5$ K) and the Bondi–Hoyle–Lyttleton model for the hot gas component ($T > 10^5$ K). Finally, BHs release energy proportionally to their accretion rate. AGN feedback is modelled in one or two modes, and the released energy can be e.g. thermal and/or kinetic. Illustris employs a two-mode feedback, both with release of thermal energy (Sijacki et al. 2015) and a transition for $f_{\rm Edd} = 0.05$. TNG uses a two-mode feedback: thermal in the high-accretion mode and kinetic in the low-accretion mode (Weinberger et al. 2017). The transition between modes takes place at $f_{\rm Edd} = \min(2 \times 10^{-3} \times (M_{\rm BH}/10^8 \, {\rm M}_{\odot})^2, 0.1)$. Horizon-AGN uses a thermal mode for high-accretion BHs and a kinetic mode for lowaccretion BHs, with a transition at $f_{\rm Edd} = 0.01$ (Dubois et al. 2016). EAGLE employs a single thermal mode (Schaye et al. 2015). Finally, SIMBA uses two different kinetic modes with a transition at $f_{Edd} =$ 0.2 (with a maximum jet speed reached for $f_{\rm Edd} = 0.02$). A complete description of these models can be found in Habouzit et al. (2020).

In this paper, we only consider AGNs in galaxies that are well resolved in all the simulations, i.e. galaxies with a total stellar mass of $M_{\star} \ge 10^9 \, \mathrm{M_{\odot}}$.

2.2 Computation of AGN luminosity

We compute the luminosity of the BHs following the model of Churazov et al. (2005), i.e. explicitly distinguishing radiatively efficient and radiatively inefficient AGNs. The bolometric luminosity of radiatively efficient BHs, i.e. with an Eddington ratio of $f_{\rm Edd} = \dot{M}_{\rm BH}/\dot{M}_{\rm Edd} > 0.1$, is defined as

$$L_{\rm bol} = \frac{\epsilon_{\rm r}}{1 - \epsilon_{\rm r}} \dot{M}_{\rm BH} c^2. \tag{1}$$

Most of the studies based on large-scale cosmological simulations have computed the luminosity of AGNs assuming that all the AGNs were radiatively efficient, i.e. using equation (1).

BHs with smaller Eddington ratios, $f_{\rm Edd} \leq 0.1$, are considered to be radiatively inefficient and their bolometric luminosities are computed as

$$L_{\text{bol}} = 0.1 L_{\text{Edd}} (10 f_{\text{Edd}})^2 = (10 f_{\text{Edd}}) \epsilon_r \dot{M}_{\text{BH}} c^2.$$
 (2)

The hard X-ray luminosities are then computed by applying the bolometric correction (BC) of Hopkins, Richards & Hernquist (2007):

$$\log_{10} L_{2-10 \text{ keV},\odot} = \log_{10} L_{\text{bol},\odot} - \log_{10} BC, \tag{3}$$

with

$$BC = 10.83 \left(\frac{L_{\text{bol},\odot}}{10^{10} \, \text{L}_{\odot}} \right)^{0.28} + 6.08 \left(\frac{L_{\text{bol},\odot}}{10^{10} \, \text{L}_{\odot}} \right)^{-0.020}. \tag{4}$$

Recently, however, Duras et al. (2020) showed that the hard X-ray correction could be slightly lower than the Hopkins et al. (2007) correction in the range $\log_{10} L_{\rm bol} = 10^{10.5} - 10^{12.5} \, \rm L_{\odot}$. Using the correction of Duras et al. (2020) changes the hard X-ray luminosity function of the simulations, which is slightly shifted towards more luminous AGN, but does not affect the conclusions of this paper. We discuss this in Section 4.1.

3018 M. Habouzit et al.

We use the radiative efficiency parameter that has been used to derive the accretion rate self-consistently in the simulations. Therefore, we use $\epsilon_r = 0.2$ for Illustris, TNG100, and TNG300, and $\epsilon_r = 0.1$ for Horizon-AGN, EAGLE, and SIMBA. The choice of the efficiency parameter will affect the normalization of the functions that we study here, and we discuss this aspect when needed in the different sections below. We point out that in theory the radiative efficiency depends on BH spin. All the simulations studied here employ a single fixed value of ϵ_r ; a more physical approach would be to draw values of ϵ_r from a distribution that reflects the distribution of BH spins, and this could impact the properties of BHs and AGNs. We discussed this in Habouzit et al. (2020).

2.3 AGN obscuration

In this paper, we compare the AGN population produced by the different simulations to several observational constraints. These constraints already include corrections for AGN obscuration. For that reason, we do not add any further correction for obscuration in the first sections of the paper. Thus, Figs 2–6, 8, and 9 do not include a correction for obscuration. However, in Section 6 we predict the number of AGNs that we could detect with the future X-ray upcoming or concept missions Athena, AXIS, and LynX. To do so, we correct the simulated populations of AGNs with empirically motivated models for obscuration as described below.

The gas and dust content of a galaxy and/or of the surroundings of its AGN can be the source of obscuration. Photons emanating from an AGN can be absorbed along the line of sight to the observer, and consequently the apparent luminosity of the AGN can be lower than its intrinsic luminosity. The hard (2–10 keV) band is less susceptible to obscuration, which means that Compton-thin AGNs with hydrogen column densities of $10^{22} \le N_{\rm H}/{\rm cm}^{-2} \le 10^{24}$ are not significantly impacted. However, some AGNs could be heavily obscured (i.e. Compton-thick AGN) with column densities of $N_{\rm H} \geqslant 10^{24} \, \rm cm^{-2}$ and be completely missed even by hard X-ray surveys. There is evidence showing that the Compton-thick AGN fraction could be constant with both redshift and luminosity (Buchner et al. 2015). There is also recent work indicating that Compton-thick torii could be present in all AGNs, independent of the Eddington ratio (see fig. 4 of Ricci et al. 2017; Buchner & Bauer 2017). Thus far, there is still no consensus on the amount of obscured AGNs in the Universe, and how the fraction of obscured AGNs could evolve with the AGN luminosity and/or redshift.

In order to account for obscured AGNs, we employ and test the following two different models:

- (i) First model: We simply assume that a fixed fraction of the AGNs is obscured (40 per cent).
- (ii) Second model: We follow the observational constraints of Ueda et al. (2014) and Merloni et al. (2014)¹ and build a redshift- and AGN hard X-ray luminosity-dependent fraction of obscured AGNs. Our model, shown in Fig. 1, assumes that there is an anticorrelation between the fraction of obscured AGNs and their X-ray luminosities, and that they are more numerous at higher redshift. Our model is defined as

$$f_{\text{obsc. AGN}}(L_x, z) = 0.2 + (0.5/1.66)$$

 $\times \text{erfc}[\log_{10}(L_x/(\text{erg s}^{-1})) - \alpha(z)],$ (5)

¹The observational constraints of Ueda et al. (2014) and Merloni et al. (2014) initially represent Compton-thin AGN, but the presence of Compton-thick AGN in these observations cannot be ruled out.

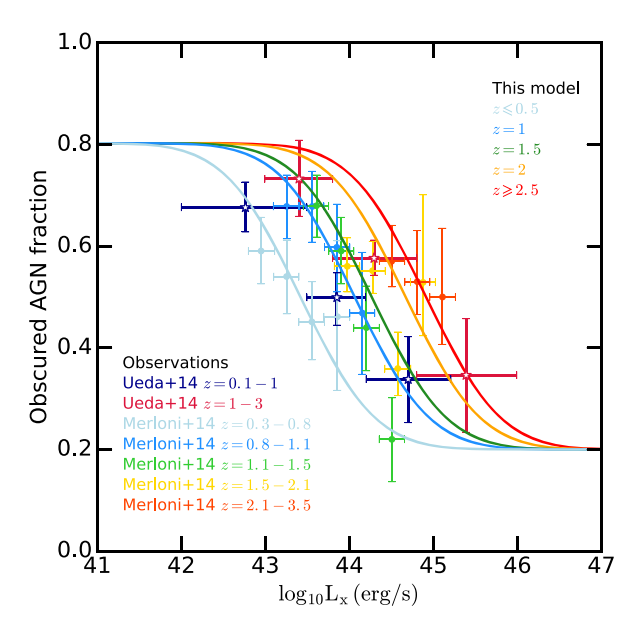


Figure 1. We use two different models for the fraction of obscured AGNs. The first model assumes that 40 per cent of the AGNs are obscured at any redshift, and independently of their luminosities. The figure shows our second model, which assumes an anticorrelation between the fraction of obscured AGNs and their hard X-ray luminosities, and more obscured AGNs at higher redshifts following the empirical results of Ueda et al. (2014) and Merloni et al. (2014).

with erfc the complementary function [erfc(x) = 1 - erf(x)], and $\alpha = 44.909$, 44.666, 44.246, 44.060, and 43.414 for $z \ge 2.5$, z = 2, z = 1.5, z = 1, and z < 1, respectively.

These models modify the luminosity and/or the number of AGNs at a given luminosity and redshift. The differences of these models are investigated in Section 6. In our models, we do not explicitly distinguish between Compton-thin and Compton-thick AGNs, but rather assume that the models represent the fraction of all obscured AGNs. For both obscuration models, we either completely remove the obscured AGNs from our samples (hereafter called the *removed* model) or we assume that their apparent hard X-ray luminosity is one order of magnitude smaller than their intrinsic luminosity (*fainter* model).

3 RESULTS: EDDINGTON RATIOS

3.1 What BHs power the AGN in different simulations?

In Fig. 2 (top panels), we show the median relation between the bolometric luminosity of the BHs (we do not restrict to AGN but rather include all BHs) and their masses, for different redshifts. At fixed BH mass, the median $L_{\rm bol}$ decreases with time (blue to red lines) for all the simulations. The median $L_{\rm bol}$ is generally the lowest in EAGLE, which produces BHs with lower average accretion rates than the other simulations. At $z \geq 2$, most of the simulations (except EAGLE) have a median bolometric luminosity at 0.1–100 per cent of the Eddington luminosity (i.e. lying between the two black lines in Fig. 2). At lower redshifts, and even more so for massive BHs, the median $L_{\rm bol}$ drops below 0.1 per cent of the Eddington luminosity. The redshift evolution of the simulations is predominantly due to the decrease of the average amount of gas available in galaxies with time, i.e. to cosmic starvation. However, the time evolution and the variations between simulations are due to the specific BH and galaxy

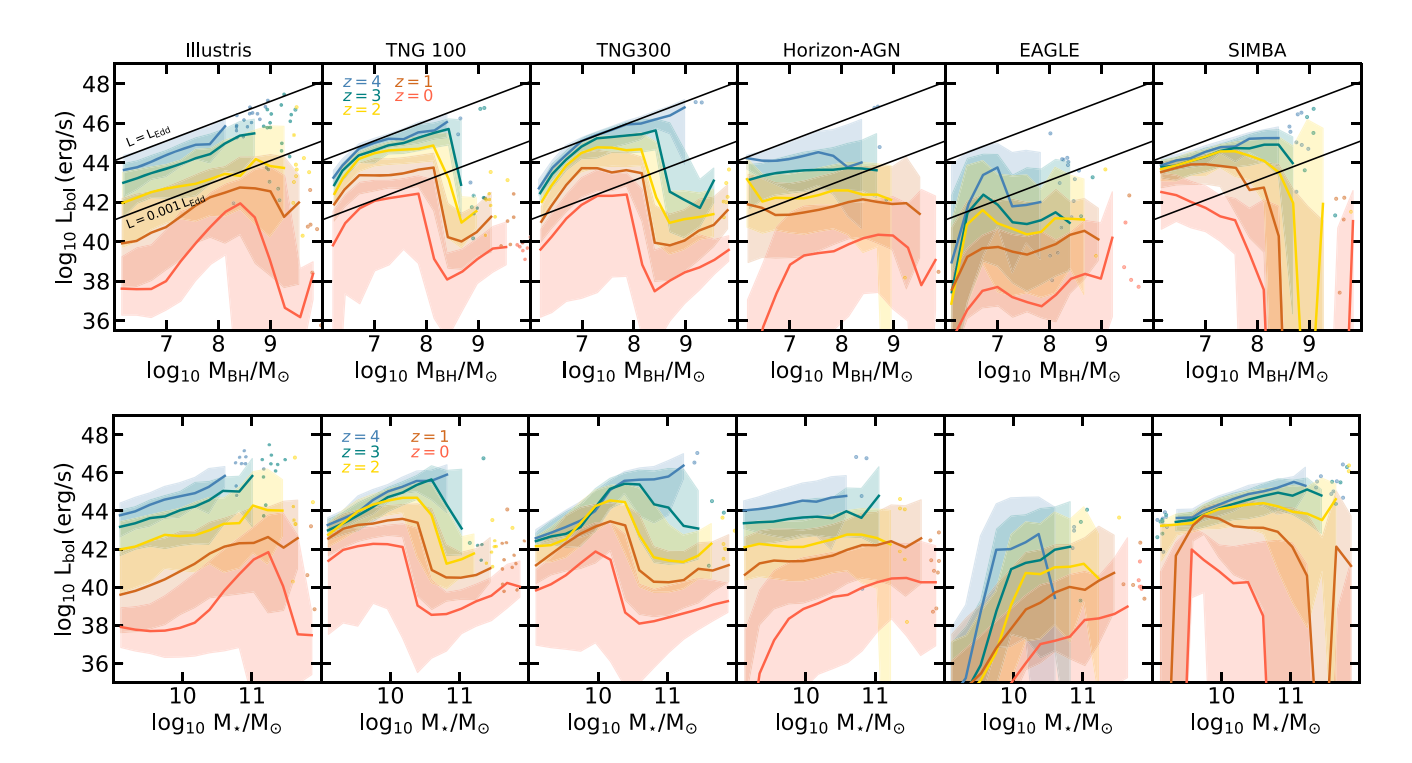


Figure 2. Top panels: Median bolometric luminosity as a function of BH masses for all the simulations, at different redshifts. Dots indicate single BHs when bins contain less than 10 BHs, and shaded areas the 15–85th percentiles of the distributions. The Eddington and 0.1 per cent Eddington luminosity are shown as black solid lines to guide the eye. Most of the simulated BH populations have, on average, luminosities lying between these two references at high redshift. At fixed BH mass, the median bolometric luminosity of the BHs decreases with time, for all the simulations. We detail the specifics of each simulation in the text. Bottom panels: Median bolometric luminosity as a function of the stellar mass of BH host galaxies.

subgrid physics of the simulations. The sharp decrease found in some simulations for massive BHs is due to AGN feedback ($M_{\rm BH} \geqslant 10^8\,{\rm M}_\odot$). This is also noticeable in the $L_{\rm bol}$ – M_{\star} plane (Fig. 2, bottom panels). Given the tight correlation between BH mass and galaxy mass in all the simulations (Habouzit et al. 2020), the median $L_{\rm bol}$ scales in the same way with $M_{\rm BH}$ and M_{\star} .

Regarding the redshift evolution, we note that Illustris, Horizon-AGN, and EAGLE have a stronger evolution than TNG and SIMBA for $M_{\rm BH} \leqslant 10^8 \, \rm M_{\odot}$. For example, the median in Illustris spans the range $\log_{10} L_{\rm bol}/(\rm erg \, s^{-1}) = 38$ –45 in the redshift range z=5–0, and only $\log_{10} L_{\rm bol}/(\rm erg \, s^{-1}) = 42$ –44 in TNG. At $z \le 2$, low-mass BHs of $M_{\rm BH} \leqslant 10^8 \, \rm M_{\odot}$ in Illustris, Horizon-AGN, and EAGLE lose their ability to accrete gas efficiently, while the same-mass BHs have about one order of magnitude higher median $L_{\rm bol}$ at higher redshift. The TNG and the SIMBA simulations produce a population of BHs with $M_{\rm BH} \leqslant 10^8 \, \rm M_{\odot}$ able to accrete gas efficiently even at low redshifts, compared to the other simulations. The quenching of BHs in satellite galaxies can be responsible for the decrease of the low-mass BH luminosity (Donnari et al. 2021).

The median luminosity decreases for massive BHs of $M_{\rm BH} \ge 10^8\,{\rm M_\odot}$ in all of the simulations (with the exception of the EAGLE simulation), and illustrates the impact of their own feedback.² In the TNG simulations, we clearly see the impact of the strong low-accretion rate state AGN feedback: AGN luminosities are strongly

reduced at all redshifts. In TNG, the transition between the highaccretion rate AGN feedback mode (injection of thermal energy) and the low-accretion rate feedback mode (kinetic mode) takes place at $f_{\rm Edd} = \min[2 \times 10^{-3} (M_{\rm BH}/10^8 \, {\rm M}_{\odot})^2, 0.1]$ (Pillepich et al. 2018; Weinberger et al. 2017). Most of the BHs with $M_{\rm BH} \gtrsim 10^8 \, \rm M_{\odot}$ (corresponding to galaxies with stellar masses of a few times $10^{10}\,\mathrm{M}_{\odot}$) have low accretion rates, and thus transition to the more efficient kinetic mode. This mode is responsible for regulating BH and star formation activity in the TNG galaxies (Weinberger et al. 2018; Habouzit et al. 2019; Li et al. 2019; Terrazas et al. 2019). We also see the effect of quenching in Illustris (which uses a different modelling of AGN feedback), but only at low redshift (z < 1). There is also a strong indirect self-regulation of AGN in SIMBA at $z \le$ 2, but starting at different BH masses for different redshifts. In SIMBA, AGN feedback heats the CGM of galaxies, which leads to their quenching. This curtails the dominant growth mode of BH torque-limited accretion, and results in an indirect self-regulation of the BHs. Indeed, BH growth in SIMBA is quenched for BHs of $M_{\rm BH} \geqslant 10^{7.5} \, {\rm M}_{\odot}$ at z = 0, but only more massive BHs get quenched at higher redshift, on average. This is likely due to the AGN feedback modelling in SIMBA, and particularly the low-accretion jet mode that is responsible for galaxy quenching and shutting down BH growth. In this AGN feedback mode, the velocity of AGN-driven winds increases for lower f_{Edd} , and only reaches maximum velocity for f_{Edd} \leq 0.02. Since Eddington ratios decrease with time even for relatively low-mass BHs of $M_{\rm BH} \leq 10^8 \, \rm M_{\odot}$ (see Fig. 3), the feedback becomes more impactful at lower BH mass with time. In other words, the $f_{\rm Edd}$ = 0.02 threshold for maximum jet velocity is reached at lower BH mass at low redshift: At z = 0, any BH with $M_{\rm BH} \ge 10^{7.5} \, \rm M_{\odot}$ can transition to the jet mode due to the low Eddington ratios; however, at higher

²To fully understand and quantify the self-regulation of AGN, running cosmological simulations with and without AGN feedback is important, but computationally expensive. This has been done for the Horizon-AGN and Horizon-noAGN (Peirani et al. 2017).

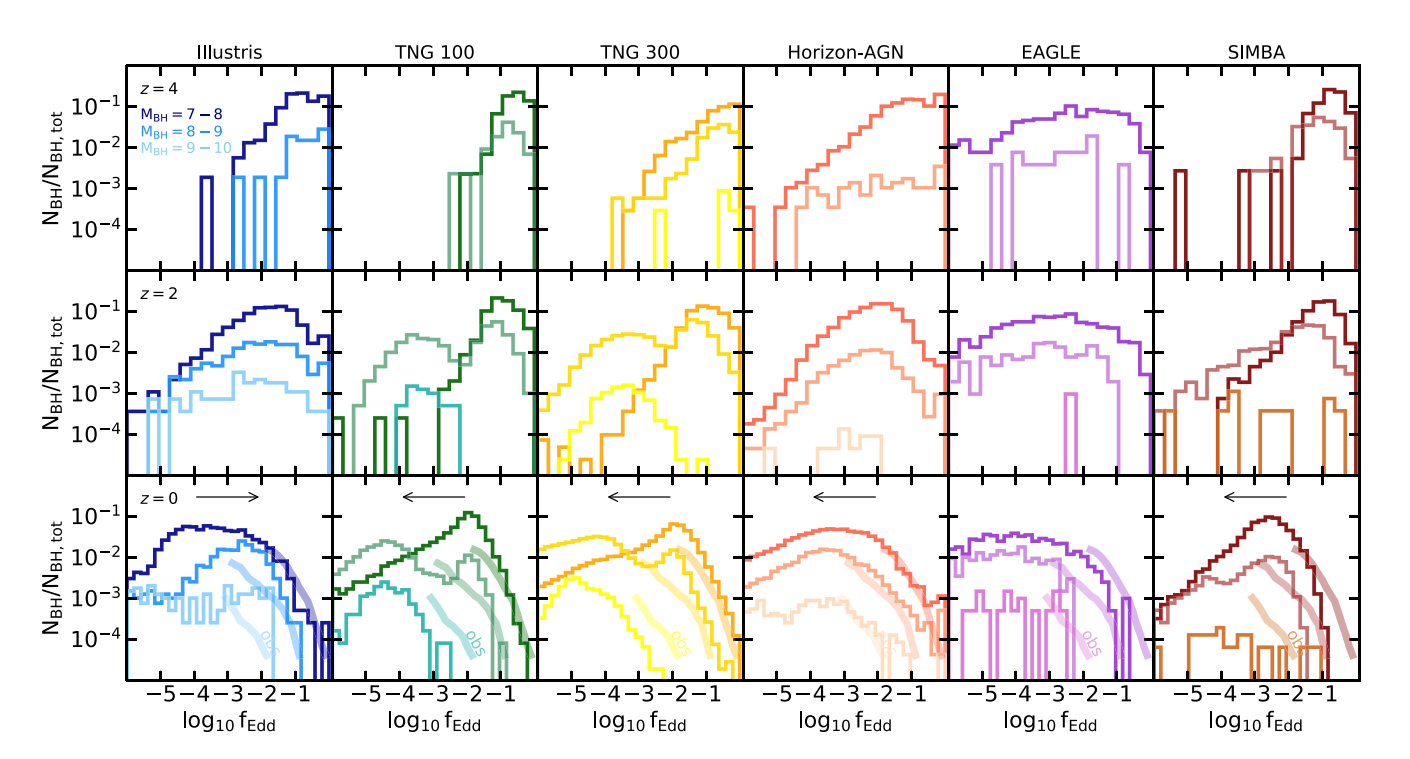


Figure 3. Eddington ratio distributions (the *y*-axes use logarithmic scales). Each bin is normalized to the total number of BHs in the three mass bins. While the peaks of the TNG100, TNG300, Horizon-AGN, and SIMBA $f_{\rm Edd}$ distributions move towards lower $f_{\rm Edd}$ for more massive BHs (as indicated by the black arrows), this is not the case for Illustris and EAGLE. Observational constraints from SDSS at z=0 (Heckman et al. 2004) are shown as thick shaded lines for the z=0 panels. There is a good agreement with the simulations for the low-mass BH bins of $M_{\rm BH}=10^{7-8}$ and $10^{8-9}~\rm M_{\odot}$. For the most massive BHs of $M_{\rm BH}=10^{9-10}~\rm M_{\odot}$, we find that the simulations either overestimate the Eddington ratios of these BHs (Illustris) or underestimate them (TNG), at z=0. We identify a strong signature (bimodal $f_{\rm Edd}$ distribution) of the transition between the two modes of the AGN feedback modelling in the TNG and SIMBA simulations.

redshifts only BHs of $M_{\rm BH} \geqslant 10^{8.5} \, {\rm M}_{\odot} \, (z=3)$ can start transitioning to the jet mode because Eddington ratios are on average high.

There is a sharp decrease in Illustris for $M_{\rm BH} \geqslant 10^8 \, \rm M_{\odot}$, but only at low redshift. We do not identify a sharp decrease of $L_{\rm bol}$ for the massive BHs in Horizon-AGN (except at z=0). In Horizon-AGN, the most massive BHs at fixed stellar mass tend to either power faint AGNs or are inactive BHs. As a result, when binned in $M_{\rm BH}$ or M_{\star} the median bolometric luminosity appears almost completely flat.

In EAGLE, the impact of AGN feedback is effective in galaxies with BHs of $M_{\rm BH} \geqslant 10^7 \, \rm M_{\odot}$ (see fig. 3 of Habouzit et al. 2020), but the effect is masked by the strong SN feedback regulating the median bolometric luminosity for the low-mass BHs. Indeed, the $L_{\rm bol}$ luminosity is reduced for both the low-mass BHs stunted by SN feedback ($M_{\rm BH} \leqslant 10^{6.5} \, \rm M_{\odot}$) and the BHs self-regulated by their feedback ($M_{\rm BH} \geqslant 10^7 \, \rm M_{\odot}$). Only BHs of $M_{\rm BH} = 10^{6.5-7} \, \rm M_{\odot}$, between the two regulation phases, power slightly brighter AGN in EAGLE.

From Fig. 2, the self-regulation of the BHs and also the quenching of the galaxies appear to be different in different simulations. While it seems to be most efficient in the TNG and SIMBA simulations with a sharp decrease of $L_{\rm bol}$ for massive BHs (see also Davé et al. 2019; Donnari et al. 2019, 2020), other simulations like EAGLE also have a strong quenching but masked by the average low $L_{\rm bol}$ for all BH masses. We emphasize here that the features and redshift evolution identified in this section also likely depend on gas availability and fuelling, in addition to the specific coupling of accretion and feedback in each simulation.

The imprint of the different subgrid models of the simulations can already be seen in the median AGN luminosity as a function of BH mass. The AGN populations predicted by different simulations are powered by different BHs.

Observational samples of AGNs with BH mass estimates from the continuum and emission lines (not dynamical mass measurements) lie in the range $L_{\rm bol}=(0.001-1)\,L_{\rm Edd}$ (i.e. the two black lines in Fig. 2). The sample of Baron & Ménard (2019) in the low-redshift Universe does not show a sharp decrease of $L_{\rm bol}$ such as the one found in some simulations for massive BHs (or similarly massive galaxies), but does show a strong $L_{\rm bol}-M_{\rm BH}$ correlation. Analyses of the relation between the AGN luminosity and the stellar mass of the host galaxies have been carried out in hard X-ray (2–10 keV) at higher redshift (z=1–2). When only selecting star-forming galaxies, a strong linear correlation was found (Mullaney et al. 2012; Aird, Coil & Georgakakis 2017) in general good agreement with the simulations for the median X-ray luminosity in galaxies with $M_{\star} \leq 10^{10.5}\,{\rm M}_{\odot}$. Aird et al. (2017) also identify a flattening at the low-mass end of the $L_{\rm x}$ – M_{\star} relation, which could hint the effect of SN feedback in these galaxies.

In massive galaxies, we compare the simulations qualitatively to the analysis of the full galaxy population of Georgakakis et al. (2017). While the normalization of the AGN luminosity is consistent with the values of Mullaney et al. (2012) and Aird et al. (2017)³ and a linear relation is found at $z \ge 2$, Georgakakis et al. (2017) identify a flattening (or slight decrease) of the relation for galaxies with $M_{\star} \ge 10^{10.5} \, \mathrm{M}_{\odot}$ for z < 2. This could be evidence of the impact of AGN feedback in massive galaxies, as seen in some simulations even if the flattening/decrease is not as strong as in the simulations. The

³These works rely on star-forming samples. Similar stellar mass and SFR samples are needed to compare these constraints to simulations. We investigate this in the next paper of our series.

flattening of the relation at the massive end is indeed seen in massive galaxies with reduced sSFR at z=1 and 2 (see Fornasini et al. 2018, for the relation between the galaxy total X-ray luminosity and galaxy stellar mass). However, there is no consensus yet, as Carraro et al. (2020) recently find a linear increasing relation with stellar mass for quiescent massive galaxies up to z=3 (shallower relation than for star-forming galaxies). This highlights the potential discrepancies with simulations showing a strong decrease due to AGN feedback in massive galaxies. The above comparisons are qualitative as we do not apply here the same detection limits and selection biases as these observational studies.

3.2 Eddington ratio distributions

The evolution of accretion rates on to BHs of different masses is key to understanding not only how the BH population grows with time statistically but also how BHs can self-regulate through AGN feedback. The accretion on to BHs is connected to two quantities. The first one is the radiative efficiency $\epsilon_{\rm r}$ that quantifies the fraction of accreted mass radiated away, and therefore links the growth of BHs to their bolometric luminosity. The second parameter is the Eddington ratio $f_{\rm Edd} = \dot{M}_{\rm BH}/\dot{M}_{\rm Edd} = L_{\rm bol}/L_{\rm Edd}$, linking the bolometric luminosity of the BHs to the Eddington luminosity $L_{\rm Edd} = 4\pi c Gm_{\rm H} M_{\rm BH}/\sigma_{\rm T}$.

We show in Fig. 3 the distribution of the BH Eddington ratios binned in three BH mass bins: $\log_{10} M_{\rm BH}/M_{\odot} = 7-8, 8-9$, and 9–10. All distributions are normalized to the total number of BHs in the simulations (and not by the number of BHs in a given BH mass bin), in order to compare with the observational constraints of Heckman et al. (2004). Varying our choice of the bin size slightly alters the normalization of the distributions, but not our conclusions below. We find that the simulations present several different important features, which we detail in the following. We find that all the simulations studied here peak at different Eddington ratios at fixed BH mass bins and redshift: e.g. for $\log_{10} M_{\rm BH}/M_{\odot} = 7-8$ at z=0, $\log_{10} f_{\rm Edd,peak} \sim -4$, -2, -2, -3, -4, and -2.5 for Illustris, TNG100, TNG300, Horizon-AGN, EAGLE, and SIMBA, respectively.

3.2.1 Time evolution in a given BH mass bin

For all the simulations, the $f_{\rm Edd}$ distributions within the fixed BH mass bins of $\log_{10} M_{\rm BH}/\rm M_{\odot} = 7{\text -}8, 8{\text -}9, \text{ and }9{\text -}10 \text{ move to lower}$ Eddington ratios $f_{\rm Edd}$ with time. From z=4 to 0, the peaks of the distributions shift from by between one order of magnitude in $f_{\rm Edd}$ up to several orders of magnitude, depending on the simulation. In general, the ability of the simulated BHs, at a given $M_{\rm BH}$, to accrete gas diminishes with time.

3.2.2 Evolution across BH mass bins

The ability of a population of BHs to accrete also depends on their masses, and we focus on z=0 in the following to describe our results. For most of the simulations (TNG, Horizon-AGN, and SIMBA), we find that the mean of the Eddington ratio distributions moves towards lower ratios for more massive BHs: More massive BHs globally accrete proportionally at lower rates than their less massive counterparts. We add arrows on Fig. 3 at z=0 to illustrate the effect. In Illustris, we find the opposite trend: The distribution for BHs in the range $M_{\rm BH}=10^{8-9}\,{\rm M}_{\odot}$ peaks at a higher Eddington ratio than the distribution for $M_{\rm BH}=10^{7-8}\,{\rm M}_{\odot}$. In EAGLE, while the Eddington

ratio distributions of all BH mass bins extend to low Eddington ratios, there is no clear evolution of the mean of the distributions with the BH mass bins. Massive BHs in EAGLE do not on average accrete less gas; this can be seen in Fig. 2 with e.g. more massive BHs being more luminous at z=0.

The TNG and SIMBA simulations produce a bimodal Eddington distribution for the intermediate BH mass bin ($M_{\rm BH}=10^{8-9}\,{\rm M}_{\odot}$) for $z\leq 2$ (only in the z=0 panel for SIMBA). This bimodality reflects the transition between two modes of AGN feedback in these simulations. BHs transition from the high-accretion mode at high redshift (i.e. when BHs have high $f_{\rm Edd}$ ratios) to the low-accretion mode at lower redshift (i.e. when BHs have lower $f_{\rm Edd}$ ratios).

In TNG, the peak at $\log_{10} f_{\rm Edd} \sim -2$ corresponds to BHs in the high-accretion thermal mode of the feedback. When reaching the characteristic mass of $\log_{10} M_{\rm BH}/\rm M_{\odot} \sim 8$, many of these BHs transition to the kinetic low-accretion feedback. This mode being more efficient by design (Weinberger et al. 2018; Habouzit et al. 2019), the BHs accrete at lower rates (lower f_{Edd}), leading to the appearance of the second peak at $\log_{10} f_{\rm Edd} \sim -4$ at $z \leq 2$. This second peak is more prominent at z = 0 than z = 2 since with time more and more BHs in the mass bin $M_{\rm BH}=10^{8-9}\,{\rm M}_{\odot}$ transition to the efficient AGN feedback mode. In SIMBA, the velocity of the AGN winds scales with BH mass for the high-accretion rate mode $(f_{\rm Edd} > 0.2; \text{Dav\'e et al. 2019})$. For lower accretion rates, the velocity is further increased by a factor that is inversely proportional to the Eddington ratio, so that the feedback is stronger for lower Eddington ratios. By design, only BHs with $M_{\rm BH} \geqslant 10^{7.5} \, \rm M_{\odot}$ can enter the lowaccretion rate AGN feedback regime. The peak of the distribution at $\log_{10}f_{\rm Edd} \sim -4$ for BHs of $M_{\rm BH} = 10^{8-9}\,{\rm M}_{\odot}$ represents the BHs that have already transitioned to this strong mode of the AGN feedback modelling in SIMBA.

The transition between AGN feedback modes in Horizon-AGN and Illustris does not produce such strong signatures in the Eddington ratio distributions for our intermediate $M_{\rm BH}$ bin. However, these two simulations tend to have two-peaked distributions for more massive BHs ($M_{\rm BH}=10^{9-10}\,{\rm M}_\odot$) at z=0, which is not found for the other simulations. Indeed, in the z=0 panel of Illustris, the BHs with $M_{\rm BH}=10^{9-10}\,{\rm M}_\odot$ peak at $\log_{10}f_{\rm Edd}\sim-5$ and -2. The same trend is found in Horizon-AGN with peaks at $\log_{10}f_{\rm Edd}\sim-6$ and -3.5. The Eddington ratio distributions of the other simulations for these massive BHs on average peak at $\log_{10}f_{\rm Edd}\sim-4.5$.

3.2.3 Comparison to observational constraints

We compare the distributions to observations from Sloan Digital Sky Survey (SDSS) at $z\sim 0$ (Heckman et al. 2004; thick shaded lines in the bottom panels of Fig. 3). For the lowest BH mass bin ($\log_{10}M_{\rm BH}/\rm M_{\odot}=7$ –8), the simulations are globally in agreement with the SDSS observations. However, since the observations only probe the high-Eddington ratio tail of the $f_{\rm Edd}$ distribution (i.e. $\log_{10}f_{\rm Edd}\geq -2$), we cannot make any strong statement regarding the modelling of the simulations here. The Illustris and Horizon-AGN simulations are in good agreement with Heckman et al. (2004) in the range $\log_{10}f_{\rm Edd}\geq -2$. We note that the TNG simulations may produce too many AGNs with $\log_{10}f_{\rm Edd}\sim -2$ with $\log_{10}M_{\rm BH}/\rm M_{\odot}=7$ –8, while the EAGLE and SIMBA simulations may not form enough AGNs with $\log_{10}f_{\rm Edd}=-2$ and -1.

The Eddington ratio distributions of more massive BHs in the range $\log_{10} M_{\rm BH}/\rm M_{\odot} = 8-9$ start deviating from the constraints of Heckman et al. (2004). The Illustris, TNG, and SIMBA distributions peak at higher $f_{\rm Edd}$ than found in SDSS. The agreement is better

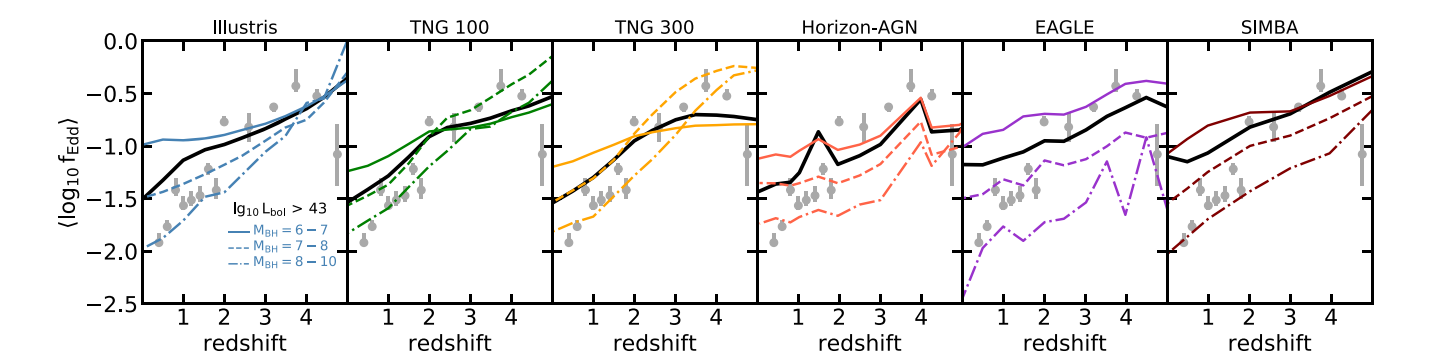


Figure 4. Black lines show the mean of the logarithm of the Eddington ratio distributions as a function of redshift. For each simulation, we show the contributions of different mass BH populations, i.e. $\log_{10} M_{\rm BH}/M_{\odot} = 6-7$, 7-8, and 8-10 (coloured solid, dashed, and dashed–dotted lines, respectively). The mean of the Eddington ratios of all the simulations decreases with time in the redshift range z = 3-0, as suggested by the observational constraints shown here. Grey symbols are observational constraints from Shen & Kelly (2012). In both simulations and observations, only AGNs with $L_{\rm bol} \ge 10^{43}$ erg s⁻¹ are considered. To some level, the results of this figure can be connected to Fig. 3, but not entirely as we only consider AGN here.

for Horizon-AGN, EAGLE, and SIMBA for the peak of the $f_{\rm Edd}$ distribution. However, the EAGLE, and SIMBA simulations still seem not to produce enough efficient accretors with $\log_{10}f_{\rm Edd} \geq -2$ for these more massive BHs of $\log_{10}M_{\rm BH}/\rm M_{\odot} = 8-9$.

Finally, for the most massive BHs in the range $\log_{10} M_{\rm BH}/{\rm M}_{\odot} =$ 9-10 the simulations are not successful in reproducing Eddington ratio distributions that agree with observational constraints. The Illustris BH population peaks at a much higher f_{Edd} than the constraints, meaning that a large population of the massive Illustris AGNs is accreting too efficiently. The TNG BH population peaks at a lower f_{Edd} (because of the efficient kinetic AGN feedback) than the observational constraints of Heckman et al. (2004). The EAGLE and SIMBA simulations hardly produce BHs in this mass range $(\log_{10} M_{\rm BH}/{\rm M}_{\odot}=9-10)$, which leads to very poor statistics for the Eddington ratio distribution. Horizon-AGN produces a better global agreement in this BH mass bin. However, the simulation seems to overpredict the number of the most efficient accretors compared to the SDSS constraints (for all the BH mass bins). Illustris also presents this feature for the BH mass bin $\log_{10} M_{\rm BH}/\rm M_{\odot} = 7-8$. This regime of $\log_{10} f_{\rm Edd} \sim 0$ needs to be taken with a grain of salt because it suffers from poor statistics in the simulations.

3.3 Time evolution of the mean Eddington ratios of AGN

We quantify the time evolution of the mean Eddington ratio for the relatively luminous AGNs that are constrained by observations; i.e. $\log_{10} L_{\text{bol}}/(\text{erg s}^{-1}) > 43$. We show the mean Eddington ratios of the simulations as a function of redshift in Fig. 4 with a black solid line, selecting only the AGN with $\log_{10} L_{\text{bol}}/(\text{erg s}^{-1}) > 43$. To some level, the time evolution of the mean Eddington ratio can be seen in the previous Fig. 3, but not completely as here we only look at luminous AGNs to be able to compare to observational constraints. The mean value $\langle \log_{10} f_{Edd} \rangle$ moves towards lower Eddington ratios with decreasing redshift for all the simulations. This is in qualitatively good agreement with the observational constraints of Shen & Kelly (2012) in the redshift range z = 0-4 (grey symbols in Fig. 4), obtained from the analysis of \sim 60 000 SDSS DR7 AGNs (0.3 $\leq z \leq$ 5). This is also in agreement with the observational constraints presented in Kollmeier et al. (2006), Kelly et al. (2010), Schulze & Wisotzki (2010), and Kelly & Shen (2013), and also in semi-analytical models and other simulations (e.g. Hirschmann et al. 2014, and references

therein). In the constraints of Shen & Kelly (2012), there is a turnover at higher redshifts z>4 (although with large uncertainties). In our analysis, we identify this turnover in several simulations: The mean $f_{\rm Edd}$ values decrease for z>4 in Horizon-AGN, and EAGLE, but not in Illustris, TNG100, and SIMBA.

The simulations do not provide an exact quantitative agreement with observations. For example, all the simulations seem to have higher mean Eddington ratios at z < 1 than the observations, meaning that the AGNs are on average accreting more than in the observations. We also note that SIMBA and EAGLE overestimate the mean Eddington ratios for z < 2, while providing a good agreement at higher redshifts with the measurements of Kelly & Shen (2013). The higher mean Eddington ratios in SIMBA are due to both the seeding of the simulation and the accretion model. In SIMBA low-mass BH seeds of $M_{\rm BH} = 1.43 \times 10^4 \, \rm M_{\odot}$ are placed in relatively highmass galaxies (compared to other simulations) of $M_{\star} \ge 10^{9.5} \,\mathrm{M_{\odot}}$. Just after seeding, BHs are undermassive with respect to the local $M_{\rm BH}$ - M_{\star} scaling relation, i.e. undermassive for their galaxies. Since $f_{\rm Edd}$ scales with $\propto \dot{M}_{\rm BH}/M_{\rm BH}$, this results in higher Eddington ratios $f_{\rm Edd}$ for these BHs than if they would have been on the scaling relation. The torque accretion model is also almost independent of BH mass, with $\dot{M}_{\rm BH} \propto M_{\rm BH}^{1/6}$ (Anglés-Alcázar, Özel & Davé 2013; Anglés-Alcázar et al. 2015), so that young BHs catching up to get on the scaling relation can have a broad range of accretion rates (which is not the case for the Bondi accretion model scaling as $M_{\rm BH}^2$). Finally, the spikes identified in the mean f_{Edd} of Horizon-AGN are likely due to the creation of new refinement levels in the simulation grid.

3.3.1 Evolution across BH mass bins

In Fig. 4, we also show the contributions of different BH mass bins⁴ to the mean Eddington ratios $\langle \log_{10} f_{\rm Edd} \rangle$: The contributions of BHs with $M_{\rm BH} = 10^{6-7} \, \rm M_{\odot}$ are shown with coloured solid lines, those of $M_{\rm BH} = 10^{7-8} \, \rm M_{\odot}$ BHs with dashed lines, and those of $M_{\rm BH} = 10^{8-10} \, \rm M_{\odot}$ BHs with dashed dotted lines. Lower mass BHs always have higher mean Eddington ratios, for all the simulations except TNG at z > 2. In the TNG simulations, the sample composed of

⁴Only the mean Eddington ratios are presented in Shen & Kelly (2012), and not the contribution of different BH mass bins.

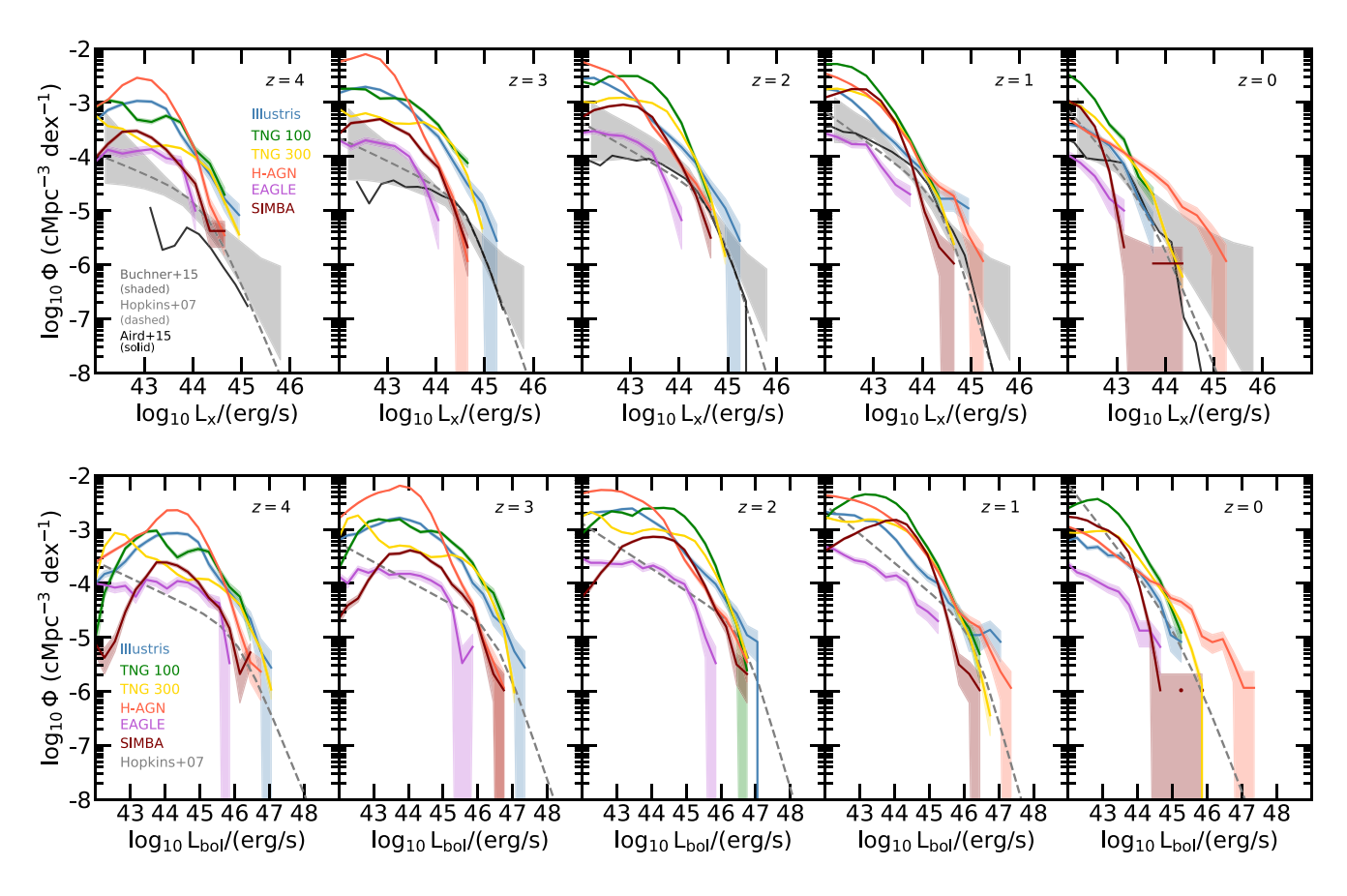


Figure 5. Top panels: Hard X-ray (2–10 keV) AGN luminosity function for the simulations (shaded areas represent Poisson error bars). No AGN obscuration model is applied to the simulations. Observational constraints are shown in grey (Hopkins et al. 2007; Aird et al. 2015; Buchner et al. 2015). The shapes of the LFs are in good agreement with the constraints. An excess of AGNs with luminosities of $\log_{10} L_x/(\text{erg s}^{-1}) \le 44$ is found in all the simulations at $z \ge 2$. This excess vanishes to some extent at lower redshifts. Most of the simulations (except Horizon-AGN) produce very few bright AGNs with $\log_{10} L_x/(\text{erg s}^{-1}) \ge 44$, in disagreement with observational constraints. EAGLE produced the lowest number of AGNs of any luminosity. As a result, the EAGLE faint end is in better agreement with the observations at $z \ge 1$ with respect to the other simulations, but it is not sufficient to reach the observational constraints at z < 1. We use the radiative efficiency $\epsilon_r = 0.2$ for Illustris and TNG, and $\epsilon_r = 0.1$ for Horizon-AGN, EAGLE, and SIMBA. Bottom panels: Bolometric AGN luminosity functions, and observational constraints in grey (Hopkins et al. 2007).

more massive BHs of $M_{\rm BH} \geqslant 10^7 \, \rm M_{\odot}$ has higher Eddington ratios at $z \ge 2$ than the BHs of $M_{\rm BH} = 10^{6-7}\,{\rm M}_{\odot}$. As shown in our previous paper (e.g. fig. 5 of Habouzit et al. 2020, with the time evolution of the median $M_{\rm BH}$ – M_{\star} relation), the stronger SN feedback of the TNG simulations implies that the initial growth of the TNG BHs is delayed (particularly for $z \ge 2$), compared to the Illustris BHs for example. These BH seeds are not able to accrete, and therefore have, on average, lower Eddington ratios than more massive BHs. While the $\langle \log_{10} f_{\rm Edd} \rangle$ means are relatively high in Illustris and TNG for massive BHs of $M_{\rm BH}=10^{7-8}$ and $10^{8-10}\,{\rm M}_\odot$ at high redshift z > 2, this is not the case for Horizon-AGN, EAGLE, and SIMBA. The EAGLE simulation shows an interesting behaviour: While the efficient AGNs powered by low-mass BHs of $M_{\rm BH}=10^{6-7}\,{\rm M}_{\odot}$ have very high $\langle \log_{10} f_{\rm Edd} \rangle$ compared to most of the other simulations, the ones powered by more massive BHs of $M_{\rm BH}=10^{8-10}\,{\rm M_\odot}$ have the lowest mean Eddington ratios through cosmic time, below the other simulations.

We have demonstrated here that while the redshift evolution of the mean $\langle \log_{10} f_{\rm Edd} \rangle$ of the simulated AGN with $\log_{10} L_{\rm bol}/({\rm erg \, s^{-1}}) >$ 43 is similar for all the simulations, the evolution for different BH mass bins varies from simulation to simulation owing to variations in subgrid modelling.

4 RESULTS: NUMBER DENSITY OF AGN

4.1 Bolometric and hard X-ray (2–10 keV) AGN luminosity functions

The AGN luminosity function is one of the fundamental quantities that characterize the demographics of active BHs. It represents the AGN comoving space density as a function of their luminosity. We show the hard X-ray (2–10 keV) and bolometric luminosity functions in Fig. 5. As described in section 2.6 of Habouzit et al. (2020), none of the simulations studied here have been calibrated with the AGN luminosity function, thus making them true predictions of the simulations. To derive the hard X-ray AGN luminosities, we used the BC of Hopkins et al. (2007). We also tried the new correction of Duras et al. (2020), which slightly shifts the AGN luminosity functions of the simulation towards more luminous AGN, as shown in Fig. A1 (bottom panels), without affecting the conclusions that we draw below.

In this section, we compare the AGN luminosity functions from the simulations to the observed X-ray luminosity functions of Buchner et al. (2015) and Aird et al. (2015). We also add the analysis of Hopkins et al. (2007); i.e. we translate their bolometric luminosity function into hard X-ray constraints (in the same way as for the

simulated AGN in Section 2.2). Since the empirical luminosity functions include corrections for Compton-thick and Compton-thin AGNs, we do not add any corrections for AGN obscuration to the simulation data in this section.

For clarity, we show only the three measurements discussed above in Fig. 5, but many more constraints have been derived for low and high redshifts (Aird et al. 2008, 2010, 2015; Lusso et al. 2012; Ueda et al. 2014; Vito et al. 2014, 2016; Georgakakis et al. 2015; Giallongo et al. 2015; Miyaji et al. 2015; Koulouridis et al. 2018; Ananna et al. 2019, and references therein). At z = 0, all the observations agree at a good level with the luminosity function of Buchner et al. (2015). A slightly lower normalization was recently found in Ananna et al. (2019) at z = 0.1 for $L_x > 10^{44.5}$ erg s⁻¹ (with a good agreement at higher redshift). The bright end of the luminosity function could have a slightly lower normalization for these luminosities for $z \leq 3$, as found by studies based on larger surveys than Buchner et al. (2015). The discrepancies start emerging at higher redshifts, especially at $z \ge 4$. For example, the luminosity functions of Aird et al. (2010), Ueda et al. (2014), and Vito et al. (2014, 2016) have lower normalization than the one from Buchner et al. (2015). The lower normalization compared to Buchner et al. (2015) is even more pronounced at the faint end of the luminosity function from Georgakakis et al. (2015) ($L_x < 10^{44} \,\mathrm{erg \, s^{-1}}$), or for the bright end of Giallongo et al. (2015) $(L_x > 10^{44} \,\mathrm{erg \, s^{-1}})$. The constraints of e.g. Vito et al. (2014) and Georgakakis et al. (2015) could be more reliable at $z \ge 4$ as they are based on soft X-ray selection. In summary, there are still some differences among the measurements.

In the following, we analyse the results for the hard X-ray AGN luminosity functions (Fig. 5), yet we find similar results for the bolometric luminosity function.

4.1.1 Luminosity functions at z = 0

We find a generally good agreement between the hard X-ray AGN luminosity functions from the simulations and the observations at z=0 (right-hand panel in Fig. 5). We note that TGN100 produces an excess of faint AGNs with $L_{\rm x} \leqslant 10^{43.5}\,{\rm erg\,s^{-1}}$ compared to the measurements, while EAGLE underestimates the number of these AGNs. SIMBA also produces a lower number of AGNs in the range $L_{\rm x}\sim 10^{43}-10^{44}\,{\rm erg\,s^{-1}}$ at z=0. Regarding the bright end of the hard X-ray luminosity function, we find that Horizon-AGN is the simulation producing the brightest AGN ($L_{\rm x}\geqslant 10^{44}\,{\rm erg\,s^{-1}}$), in agreement with the observations of Buchner et al. (2015) (but too many AGNs at these luminosities compared to the constraints of Aird et al. 2015). EAGLE has a harder time producing these powerful AGNs, at any redshift.

4.1.2 Luminosity functions at higher redshift

The agreement with the observations becomes weaker towards higher redshifts ($z \ge 1$). Most of the simulations have a peak in their luminosity function in the range $L_x = 10^{42} - 10^{43.5}$ erg s⁻¹ (depending on the simulation and redshift). Most of the simulations (except EAGLE) overpredict the number of AGNs with $L_x \le 10^{44}$ erg s⁻¹, by up to one order of magnitude compared to the constraints of Buchner et al. (2015), Aird et al. (2015), and Hopkins et al. (2007). However, these simulations remain in good agreement for brighter AGNs.

EAGLE shows the opposite trend, better matching the faint end of the luminosity function given its lower normalization, but EAGLE does not produce enough bright AGNs with $L_{bol} \geqslant 10^{45} \, \mathrm{erg \, s^{-1}}$ compared to the constraints of Hopkins et al. (2007).

4.1.3 Impact of the simulation resolution in TNG

The TNG100 and TNG300 simulations allow us to study the effect of volume and resolution on the luminosity function (see also Weinberger et al. 2018). The luminosity function of TNG300 has a lower normalization for $\log_{10} L_{\rm x}/({\rm erg~s^{-1}}) \leqslant 44$ and $\log_{10} L_{\rm bol}/({\rm erg~s^{-1}}) \leqslant 45$ –46. The gas density around BHs is less accurately resolved in TNG300, which can explain the fewer AGNs at fixed AGN luminosity. The fewer number of $\log_{10} L_{\rm x}/({\rm erg~s^{-1}}) \leqslant 44$ AGNs can be seen in fig. 3 of Habouzit et al. (2020), with both fainter AGNs powered by TNG300 BHs of $M_{\rm BH} \sim 10^6 \, \rm M_{\odot}$ in galaxies of total stellar mass $M_{\star} \leqslant 10^{10} \, \rm M_{\odot}$, and by BHs of $M_{\rm BH} = 10^{6-7} \, \rm M_{\odot}$ in galaxies of $M_{\star} = 10^{10-11} \, \rm M_{\odot}$, compared to the brighter TNG100 BHs.

While TNG100 and TNG300 have similar number densities of AGN with $L_{\rm bol} \gtrsim 10^{44}\,{\rm erg\,s^{-1}}$ and $L_{\rm bol} \gtrsim 10^{46}\,{\rm erg\,s^{-1}}$, the larger volume of the TNG300 (27 times larger volume than TNG100, and about 10 times larger than Horizon-AGN and SIMBA) produces even brighter AGNs (which are not present in TNG100). The number density of these brightest AGNs is in good agreement with observations at z < 2.

4.1.4 Impact of AGN variability

Cosmological simulations offer good statistics on the AGN population, but remain limited by their resolution. In particular, the region around the BHs is not sufficiently resolved (in space and time) to capture short time-scale variability. Both the simulations that resolve the region near BHs at sub-pc scales (Novak, Ostriker & Ciotti 2011; Angles-Alcazar et al. 2020) and the observations have shown that the accretion rate on to BHs can change by orders of magnitude over short time-scales that are not resolved in largescale cosmological simulations (e.g. DeGraf et al. 2017; Gabor & Bournaud 2014, and references therein). In order to account for the impact of AGN variability on the AGN luminosity function, we modify the luminosity of each simulated AGN: We randomly draw a new AGN luminosity from a lognormal distribution centred on the initial AGN luminosity and with a width of 0.3 (Fig. 6, lefthand panels) or 0.5 dex (right-hand panels). Fig. 6 shows only one realization of the AGN luminosity functions when we apply the variability models. The impact of AGN variability is only noticeable for $L_x \geqslant 10^{43.5} \, \mathrm{erg \, s^{-1}}$ for $z \ge 1$ (and for most simulations only for brighter AGN with $L_x \geqslant 10^{44.5} \, \mathrm{erg \, s^{-1}}$), and $L_x \geqslant 10^{43} \, \mathrm{erg \, s^{-1}}$ at z = 0, and we find that this bright end of the luminosity function can be shallower for several simulations. The effect is limited for a lognormal distribution with a width of 0.3 dex, and more important for the distributions with 0.5 dex width. The largest effect is found in SIMBA, whose bright end is considerably extended to brighter AGNs for the 0.5 dex width distribution model, leading to better agreement with the constraints of Buchner et al. (2015) at z = 0. EAGLE is the simulation producing the fewest bright AGNs, and we also note a shallower bright end of the AGN luminosity function when accounting for AGN variability (see also Rosas-Guevara et al. 2016), and therefore better agreement with the measurements at all redshifts.

4.1.5 Impact of other parameters

In Fig. 6, we show the impact of the radiative efficiency ϵ_r : For Illustris, TNG100, and TNG300 (i.e. the first three rows), we show both the luminosity function with $\epsilon_r = 0.2$ (the parameter employed in the simulations) and $\epsilon_r = 0.1$ (parameter used for all the other simulations). A higher radiative efficiency increases the

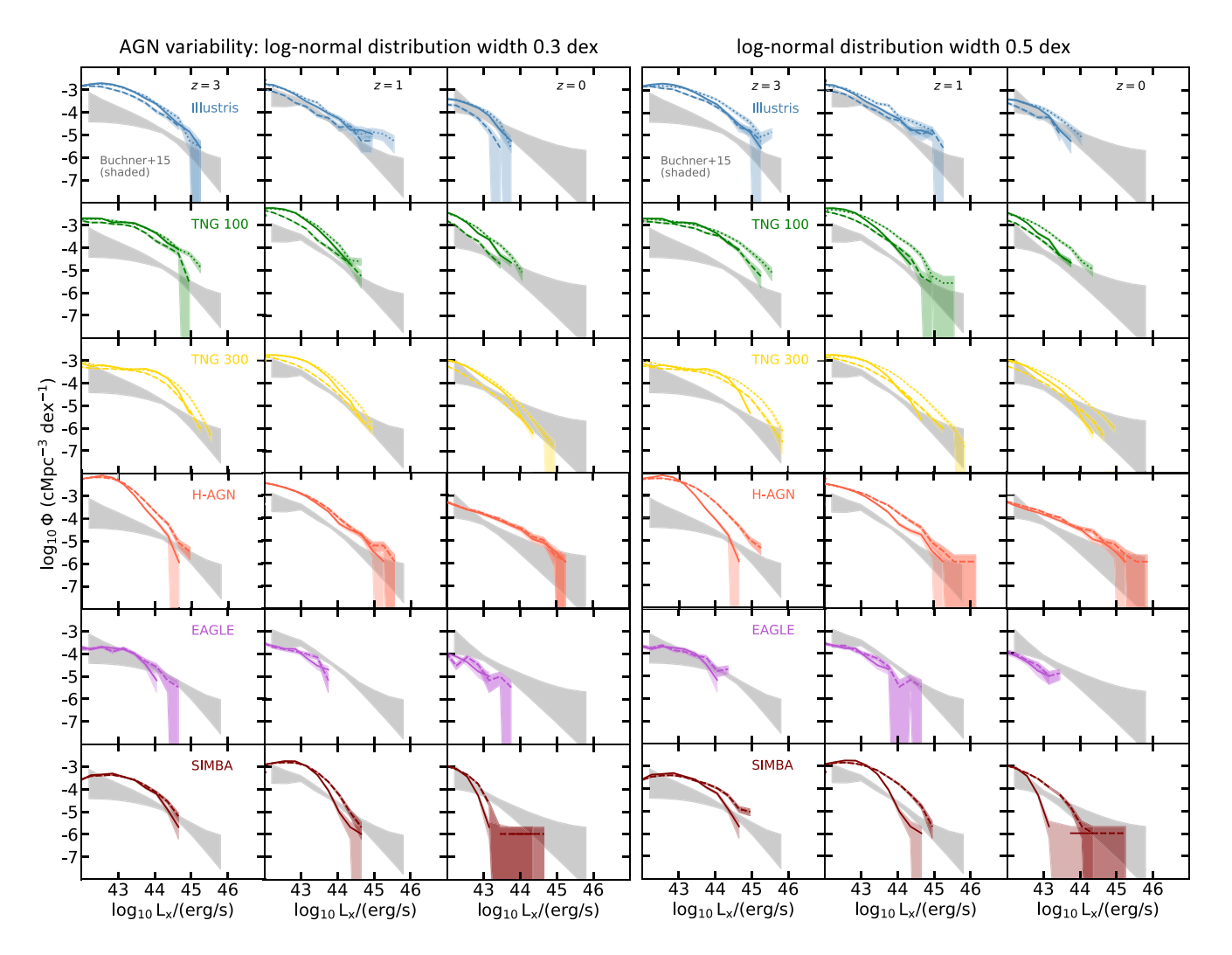


Figure 6. Hard X-ray (2–10 keV) AGN luminosity function with a correction for short time-scale AGN variability. We re-compute the luminosity of each simulated AGN by randomly selecting a new L_x from a lognormal distribution centred on the initial L_x and with a width of 0.3 dex (left-hand panels) and 0.5 dex (right-hand panels). Only one realization of the luminosity function corrected for AGN variability is shown. Solid lines show the simulation AGN luminosity function (without the variability correction) with $\epsilon_r = 0.2$ for Illustris and TNGs, and $\epsilon_r = 0.1$ for Horizon-AGN, EAGLE, and SIMBA. The dashed lines represent the luminosity function with $\epsilon = 0.1$ for all the simulations and our correction for AGN variability. This allows a direct comparison with the luminosity function of the other simulations, all having the same $\epsilon_r = 0.1$. In the panels for Illustris, TNG100, and TNG300, we also add the luminosity function computed with the AGN variability correction and $\epsilon_r = 0.2$, shown as dotted lines. The effects of AGN variability are more important for a width of 0.5 dex. In particular, the luminosity function of EAGLE is in better agreement with the observational constraints for its bright end. TNG100 and TNG300 also include now brighter AGNs, and better agree with the constraints. SIMBA also agrees better with the constraints at z = 0, but overestimates the luminosity function at higher redshifts. This figure does not include a correction for AGN obscuration for the simulations.

normalization of the luminosity functions and the number of brighter AGNs (see also appendix of Habouzit et al. 2019).

We now discuss the impact of our method to compute the AGN luminosity. In this paper, we consider that AGNs are either radiatively efficient or inefficient (see Section 2.2). The main effect of considering AGNs with $f_{\rm Edd} \leq 0.1$ as inefficient is a decrease in the amount of AGNs with $L_{\rm x} \leqslant 10^{44}~{\rm erg~s^{-1}}$, especially for $z \leq 2$ (see also appendix of Habouzit et al. 2019). To understand the role of the $f_{\rm Edd}$ transition to define efficient and inefficient AGNs, we compute the luminosity function with a transition at $f_{\rm Edd} = 0.01$ (not shown here). The main effect is also an increase of the number of AGNs with $L_{\rm x} \leqslant 10^{44}~{\rm erg~s^{-1}}$, with a lower amplitude than considering all AGNs as efficient. While most simulations are above the observational constraints (TNGs, Horizon-AGN, and Illustris) at z = 0, we find a better agreement for EAGLE and SIMBA with this $f_{\rm Edd}$ transition.

Finally, we note here that the effect of the AGN variability on the X-ray luminosity function could be similar to allowing for dispersion in the BC used to compute the hard X-ray luminosity of the AGN, and this needs to be investigated in detail. Dispersion in the conversion from X-ray to bolometric luminosities was used in Ananna et al. (2020) (following Georgantopoulos & Akylas 2010; Ueda et al. 2014) to compute the total radiation of AGN, and thus investigate the contribution of AGN to reionization.

4.2 Comoving number density of AGNs as a function of redshift

We now turn to quantify the time evolution of the number density of AGNs with different luminosities. In Fig. 7, we show the redshift evolution of the comoving number density of AGNs binned in hard

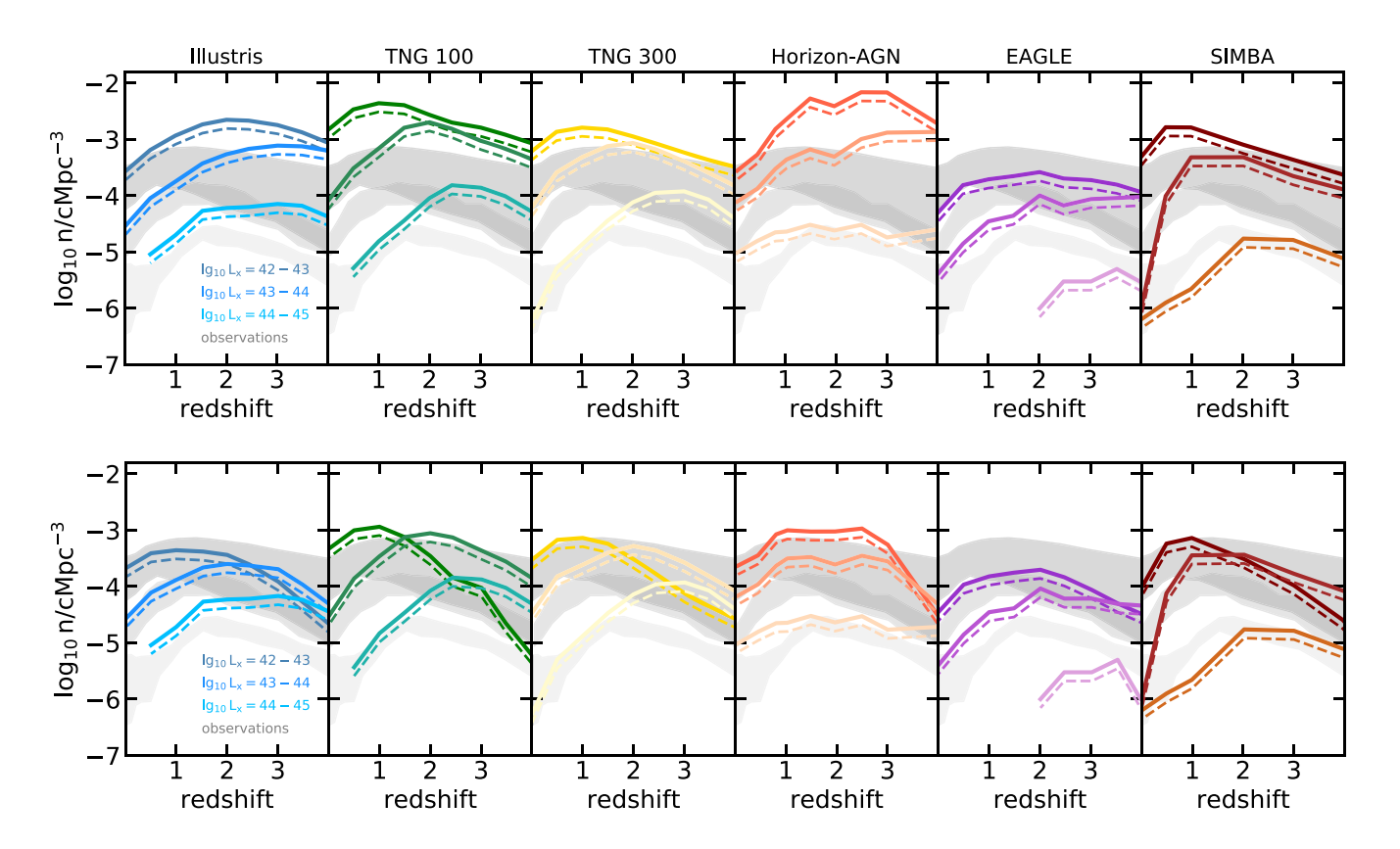


Figure 7. Top panels: Evolution of the comoving number density of AGN binned in hard X-ray luminosity, for galaxies with $M_{\star} \geqslant 10^9 \, \mathrm{M}_{\odot}$. Bottom panels: Same figure for galaxies with $M_{\star} \geqslant 10^{10} \, \mathrm{M}_{\odot}$. We show the number density (solid lines) of AGN in the luminosity bins $\log_{10} L_{\mathrm{x}}/(\mathrm{erg \, s^{-1}}) = 42-43$ (top lines), $\log_{10} L_{\mathrm{x}}/(\mathrm{erg \, s^{-1}}) = 43-44$, and $\log_{10} L_{\mathrm{x}}/(\mathrm{erg \, s^{-1}}) = 44-45$ (bottom lines). We compare the simulation data with observational constraints of Ueda et al. (2014), Aird et al. (2015), and Buchner et al. (2015): The dark grey regions correspond to the constraints for faint AGN with $\log_{10} L_{\mathrm{x}}/(\mathrm{erg \, s^{-1}}) = 42-43$, the middle grey regions to AGN of $\log_{10} L_{\mathrm{x}}/(\mathrm{erg \, s^{-1}}) = 43-44$, and the light grey regions to brighter AGN with $\log_{10} L_{\mathrm{x}}/(\mathrm{erg \, s^{-1}}) = 44-45$. In addition to the solid lines, we also show the number densities for the simulations after applying a correction for Compton-thick AGN (the most obscured AGN); dashed lines assume that 30 per cent of the simulated AGNs are Compton-thick AGN.

X-ray luminosity,⁵ considering galaxies with $M_{\star} \geqslant 10^9 \,\mathrm{M}_{\odot}$ (top panels). We show the number density (solid lines) for AGNs in the luminosity bins $\log_{10} L_{\rm x}/({\rm erg}\,{\rm s}^{-1}) = 42\text{--}43$ (top lines in each panel), $\log_{10} L_x/(\text{erg s}^{-1}) = 43-44$, and $\log_{10} L_x/(\text{erg s}^{-1}) = 44-45$ (bottom lines in each panel). A similar figure can be found in Rosas-Guevara et al. (2016) for the EAGLE simulation. Observational constraints on the number density for these AGN X-ray luminosities are shown in grey. More precisely, we show the regions enclosed by the minimum and the maximum of the three observational constraints (all together) derived by Ueda et al. (2014), Aird et al. (2015), and Buchner et al. (2015). One can see that the faint AGN regime is the one suffering from the largest uncertainties in observations, especially for $z \ge 1$. The observational constraints include a correction for moderately obscured AGNs, and therefore we do not need to correct for Compton-thin AGN ($10^{22} < N_{\rm H} < 10^{24} \, {\rm cm}^{-2}$). However, the observations do not correct for heavily obscured objects with column densities of $N_{\rm H} \geqslant 10^{24}\,{\rm cm}^{-2}$, the Compton-thick AGN. We therefore test the impact of applying an additional correction for

⁵The spikes in the AGN number density of Horizon-AGN in Fig. 7 (and in other figures of the paper) are triggered by higher levels of accretion at some given redshifts for which a new level of mesh refinement is added in the simulation. The new refinement level can also trigger spikes in the SFR history, and the effect has been discussed recently in Snaith et al. (2018).

Compton-thick AGN. The dashed lines assume that 30 per cent of the simulated AGNs are heavily obscured and we remove them from our samples. The fraction of Compton-thick AGNs is hard to constrain in observations, and could be more than 30 per cent (e.g. Gilli et al. 2007; Merloni et al. 2014). Moreover, the fraction could also depend on the AGN luminosity and redshift. The uncertainties induced by the 30 per cent heavily obscured AGNs that we use here are lower than the differences among the observational constraints.

Almost all the simulations produce too many AGNs in the range $\log_{10} L_x/(\text{erg s}^{-1}) = 42\text{--}44$ (top solid lines and top grey shaded constraints), with Horizon-AGN producing the highest number of those. However, the EAGLE simulation is in very good agreement with the observational constraints for the faint AGN of $\log_{10} L_x/(\text{erg s}^{-1}) = 42\text{--}43$ at all redshifts, but the agreement is on average poorer for more luminous AGN with $\log_{10} L_x/(\text{erg s}^{-1}) = 43\text{--}44$ (except for z=2--3). Yet the EAGLE simulation produces too few bright AGNs of $\log_{10} L_x/(\text{erg s}^{-1}) = 44\text{--}45$, at any redshift, while the other simulations produce more of these bright AGNs and obtain a better agreement with observations, at least for $z\leq 2$. Most

⁶Instead of completely removing these 30 per cent heavily obscured AGNs from our samples, we could also have decreased their luminosities by, for example, one order of magnitude. These AGNs would have moved from a given $L_{\rm x}$ bin to the fainter bin in Fig. 7.

of the simulations, except SIMBA and Horizon-AGN for which a good agreement is found, overproduce the number of these bright $\log_{10} L_x/(\text{erg s}^{-1}) = 44-45$ AGNs at high redshift $z \ge 2$. In general, we find that many of the simulations form too many AGNs of any luminosity at high redshift. This suggests that BH growth is too efficient at high redshift. Having a higher fraction of heavily obscured AGNs at high redshift would decrease the discrepancy with observations.

We can conclude here that it is hard for a given simulation to produce a number density of AGN in agreement with these observational constraints at *both* high (e.g. z > 2) and low redshifts (z < 2), but also for *both* fainter AGN [e.g. $\log_{10} L_x/(\text{erg s}^{-1}) = 42-43$] and brighter AGN [e.g. $\log_{10} L_x/(\text{erg s}^{-1}) = 44-45$]. Simulations generally reproduce one of these aspects, but fail in other regimes.

4.2.1 Peak of the AGN number density

In addition to the relative number of AGNs that we have discussed earlier, the trend with redshift is also very informative. The shape of the number density function of all the simulations is similar to the overall shape in observations: All the simulations have increasing number densities of AGN (of any luminosity) at high redshift, peak at some redshift, and then have decreasing number densities when moving towards lower redshifts. However, the redshift at which the turnover takes place is not in precise agreement with the observations for all the simulations. In observations, we see what we call the downsizing effect: brighter AGN peak (in number density) at earlier times (Ueda et al. 2014; Aird et al. 2015) and fainter AGN at later times. We also find this trend in the simulations, in a clear way for TNG and SIMBA, and in a less obvious way for the Illustris, Horizon-AGN, and EAGLE simulations. The TNG number density of AGN with $\log_{10} L_x/(\text{erg s}^{-1}) = 42-44$ peaks at roughly the same redshift as in the observations. The brightest AGN population with $\log_{10} L_{\rm x}/({\rm erg \, s^{-1}}) = 44-45$ peaks at much earlier times ($z \sim 2.5-3$) in the simulations than in observations ($z \sim 1.5-2$).

4.2.2 Uncertainties: the impact of galaxy stellar mass limits

The galaxy stellar mass limit considered above is the first aspect that could affect our comparison with observations. In the top panels of Fig. 7, we have only included AGN in galaxies of $M_{\star} \ge 10^9 \,\mathrm{M_{\odot}}$ to homogenize the resolution limit over all the simulations. The differences between simulations and observations could thus arise if the observational samples include lower mass galaxies. This is unlikely since these galaxies are difficult to detect in optical wavelengths, which is needed to estimate their redshift. Indeed, in observational samples most X-ray-detected AGNs are found to reside in more massive galaxies than $M_{\star} \ge 10^9 \,\mathrm{M}_{\odot}$, e.g. in galaxies with $M_{\star} \geqslant 10^{10} \, \mathrm{M}_{\odot}$ (Brusa et al. 2009; Xue et al. 2010; Aird et al. 2012, 2013; Mendez et al. 2013; Aird, Coil & Georgakakis 2018). We apply this latter stellar mass cut to compute the number density of the AGN in Fig. 7 (bottom panels). Considering only galaxies with $M_{\star} \geqslant$ $10^{10} \, \mathrm{M}_{\odot}$ significantly affects the results: (i) the number density of the faint AGN with $\log_{10} L_x/(\text{erg s}^{-1}) = 42-43$ is reduced, particularly at high redshift, leading to a better agreement with observational constraints for all the simulations; (ii) with a smaller amplitude, the number density of AGN with $\log_{10} L_x/(\text{erg s}^{-1}) = 43-44$ is also reduced, but they are still overproduced in simulations with respect to the observations; and (iii) the number of the brightest AGN is not affected. Many faint to intermediate AGNs in the simulations are located in galaxies with stellar mass in the range

 $M_{\star}=10^9-10^{10}~\rm M_{\odot}$, causing the changes described above. In other words, some simulations produce too many faint AGNs (especially at high redshift) in low-mass galaxies of $M_{\star}=10^9-10^{10}~\rm M_{\odot}$. Overall, these changes do not affect our main conclusion that all the simulations generally do not agree with observational constraints in all the regimes (faint/bright AGN, low/high redshift). We investigate the correlations between AGN, host galaxies, and redshift in the next paper of our series.

4.2.3 Uncertainties: obscuration effects

AGN obscuration could also trigger differences between the observations and simulations. If obscuration of Compton-thick AGN mainly arises from large amounts of gas and/or dust in the AGN host galaxies rather than small regions close to the AGN (but see Buchner & Bauer 2017), a fixed fraction of Compton-thick AGNs (as we use here) would also be an overly simplistic approach, and would affect the shape and normalization of the number density. Similarly, observations could also underestimate the number of Compton-thick AGNs due to small-scale obscuration, particularly at low luminosity.

5 RESULTS: AGN FRACTION IN GALAXIES

5.1 Time evolution of the galaxy AGN fraction

In Fig. 8 (top panels), we show the fraction of AGN with $L_{\text{bol}} \geqslant$ 10⁴³ erg s⁻¹ in galaxies of different masses as a function of redshift. This limit represents more or less the peak of the AGN bolometric luminosity function (it depends on the simulations and redshift), and allows us to include the AGN that could be detectable by the current available instruments (e.g. Chandra and XMM-Newton). Here, we define the AGN fraction as the number of galaxies hosting an active BH divided by the number of galaxes hosting a BH (active or not); we do not include galaxies that do not host a BH. To understand how the AGN occupation depends on the host galaxies. we divide the simulated galaxies into three samples with different stellar masses: $M_{\star} \sim 10^9 \, \mathrm{M}_{\odot}$ (solid lines), $M_{\star} \sim 10^{10} \, \mathrm{M}_{\odot}$ (dashed lines), and $M_{\star} = 10^{11} \, \mathrm{M}_{\odot}$ (dotted-dashed lines). In the bottom panels of Fig. 8, we instead split the data into BH mass bins: $M_{\rm BH} \sim$ $10^6 \,\mathrm{M}_\odot$ (solid lines), $M_{\mathrm{BH}} = 10^7 \,\mathrm{M}_\odot$ (dashed lines), $M_{\mathrm{BH}} = 10^8 \,\mathrm{M}_\odot$ (dashed–dotted lines), and $M_{\rm BH}=10^9\,{\rm M}_\odot$ (solid lines).

The fraction of AGN is always higher at high redshifts, for all the galaxy stellar mass bins. The increase with redshift up to $z\sim$ 3 was also found in observations for galaxies with $M_{\star} \ge 10^{9.5} \,\mathrm{M}_{\odot}$ (Aird et al. 2018). The fraction of AGN varies strongly from one simulation to another. In Illustris, TNG100, Horizon-AGN, and SIMBA,⁷ all galaxies with $M_{\star} \sim 10^9$ and $10^{10} \, \mathrm{M}_{\odot}$ have a probability of > 80 per cent to host an efficient accretor at $z \sim 4$. In EAGLE, the fraction of galaxies hosting an AGN is always lower than the other simulations, as discussed in the following. With time, the fraction of galaxies hosting efficient accretors decreases. This decrease can be linear with redshift: In Illustris, the AGN fractions decrease with the same slope from z = 4 to 0. We can also identify some different trends in the other simulations. As discussed with Fig. 2, the evolution with time of the median L_{bol} in TNG100, TNG300, and SIMBA for BHs of $M_{\rm BH} \leqslant 10^8 \, \rm M_{\odot}$ is mild for $z \ge 2$ compared to the evolution in Illustris and Horizon-AGN. As a consequence, TNG100, TNG300,

⁷In Fig. 8, we show the AGN fractions in galaxies of $M_{\star} \sim 10^9 \, \rm M_{\odot}$ for SIMBA, but we do not discuss this in the text since the BH seeding generally takes place in galaxies of $M_{\star} \sim 10^{9.5} \, \rm M_{\odot}$ in this simulation.

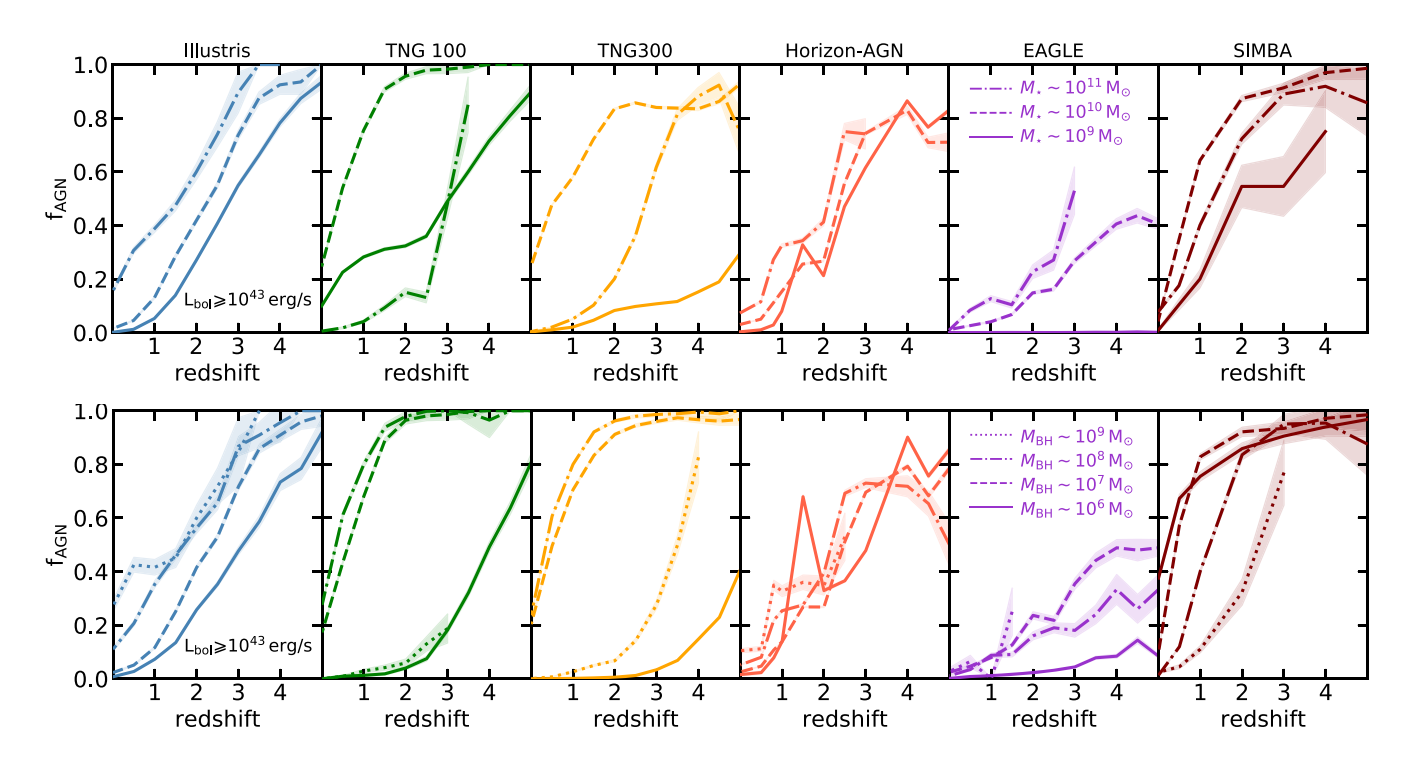


Figure 8. Fraction of AGN with $L_{\rm bol} \ge 10^{43}\,\rm erg\,s^{-1}$ in galaxies of different masses $M_{\star} \sim 10^9,\ 10^{10}$, and $10^{11}\,\rm M_{\odot}$ (top panels), and similarly different BH masses of $M_{\rm BH} \sim 10^6,\ 10^7,\ 10^8$, and $10^9\,\rm M_{\odot}$ (bottom panels). Only redshift bins with more than five galaxies are included here. Shaded areas represent Poisson error bars. The fractions of AGN are higher at higher redshifts for all the simulations, but there is no consensus on the time evolution of the AGN fractions for different ranges of BH or galaxy masses.

and SIMBA present a relatively small decrease of the AGN fractions in the redshift range z=4–2 for $M_{\star}\geqslant 10^{10}\,{\rm M}_{\odot}$. After this (z<2), the decrease of the AGN fractions is more pronounced in these simulations.

For more massive galaxies of $M_{\star} \sim 10^{11} \, \mathrm{M}_{\odot}$ (dashed-dotted lines), the fraction of AGN is even lower in TNG100/TNG300 and SIMBA. We find that the strong AGN feedback operating in the massive TNG100/TNG300/SIMBA galaxies self-regulates the BHs and significantly decreases the number of rapid accretors at redshift $z \leq 3$. From the bottom panels of Fig. 8, we see that these BHs are among the most massive with masses of $M_{\rm BH} \sim 10^9 \, \rm M_{\odot}$ for TNG100/TNG300 or $M_{\rm BH} \sim 10^8 \, \rm M_{\odot}$ for SIMBA. Interestingly, we find higher or similar fractions of AGN with $L_{bol} \ge 10^{43} \, erg \, s^{-1}$ in galaxies of $M_{\star} \sim 10^{11} \, \mathrm{M}_{\odot}$ (dashed-dotted lines) than of $M_{\star} \sim$ $10^{10} \,\mathrm{M}_{\odot}$ (dashed lines) in the Illustris, Horizon-AGN, and EAGLE simulations. This shows that at least in some simulations, massive galaxies of $M_{\star} \sim 10^{11} \, \mathrm{M}_{\odot}$ are statistically capable of feeding AGN, as the $M_{\star} \sim 10^{10} \, \mathrm{M_{\odot}}$ galaxies. In these simulations, we do not find strong differences between the fraction of AGN powered by $M_{\rm BH} \sim 10^8 \, \rm M_{\odot}$ and $M_{\rm BH} \sim 10^9 \, \rm M_{\odot}$ BHs. By z=0, the Horizon-AGN, EAGLE, and SIMBA simulations have AGN fractions of ≤10 per cent for all the galaxy mass bins presented here. This is the case for the least massive ($M_{\star} \ge 10^9 \,\mathrm{M}_{\odot}$) and most massive galaxies $(M_{\star} \geqslant 10^{11} \,\mathrm{M}_{\odot})$ of TNG100. However, the TNG100 simulation still has an AGN fraction of ~ 20 per cent in galaxies of $M_{\star} \ge 10^{10} \,\mathrm{M}_{\odot}$, which corresponds to an efficient growth phase between low gas content phases due to SN feedback and AGN feedback. We also note that the massive galaxies ($M_{\star} \geqslant 10^{11} \, \mathrm{M}_{\odot}$) in Illustris still have a high fraction of AGN (~20 per cent) due to a less efficient AGN feedback.

In EAGLE, the number of AGNs is lower than that in the other simulations, as shown in Figs 5 and 7. The AGN fraction is

<0.4 at z=4, and decreases towards lower redshifts. We note that the fraction in low-mass galaxies of $M_{\star} \sim 10^9 \, \mathrm{M_{\odot}}$ in EAGLE is close to zero for all redshifts. These low-mass galaxies host BHs of $M_{\rm BH} \sim 10^5 - 10^6 \, \mathrm{M_{\odot}}$ whose accretion is strongly stunted by SN feedback (Anglés-Alcázar et al. 2017b; Habouzit, Volonteri & Dubois 2017; McAlpine et al. 2018). SN feedback affects the growth of BHs in galaxies with $M_{\star} < 10^{10} \, \mathrm{M_{\odot}}$ from high redshift to low redshift (McAlpine et al. 2018). After the phase of SN regulation, BHs start growing in mass efficiently. At $z \geq 2$, this phase starts in galaxies of $M_{\star} \geq 10^{9.5} \, \mathrm{M_{\odot}}$ with BHs of $M_{\rm BH} \sim 10^6 \, \mathrm{M_{\odot}}$; these BHs power the ~ 10 per cent AGN fraction (bottom panel).

We have demonstrated that the fraction of efficient accretors with $L_{\rm bol} \geqslant 10^{43}~{\rm erg~s^{-1}}$ varies in time (differently in all simulations), and depends on the host galaxy stellar mass. At $z \le 2$, these differences in the fractions of galaxies hosting an AGN could help us to constrain the subgrid physics of the simulations, and particularly the efficiency of AGN feedback. We develop this point in the following subsection.

In observations, there are no clear trends in the duty cycle with galaxy or BH mass. At $z\sim0$, while Schulze & Wisotzki (2010) identify a decrease with BH mass, a mild evolution was reported in Goulding et al. (2010). More precisely, Schulze et al. (2015) find almost no evolution with BH mass for type 1 AGN with $M_{\rm BH}=10^7-10^9\,{\rm M}_\odot$ and z=1.2-2. We define AGN with a cut in the bolometric luminosity, while the definition of Schulze & Wisotzki (2010) is based on Eddington ratios. Nevertheless, we find that most simulations show an evolution of the duty cycle with BH mass in the same mass and redshift range, with the exception of EAGLE and Horizon-AGN that shows very little evolution. Schulze et al. (2015) identify a strong decrease with BH mass for lower redshift z<1.2; this trend is found in most simulations as well.

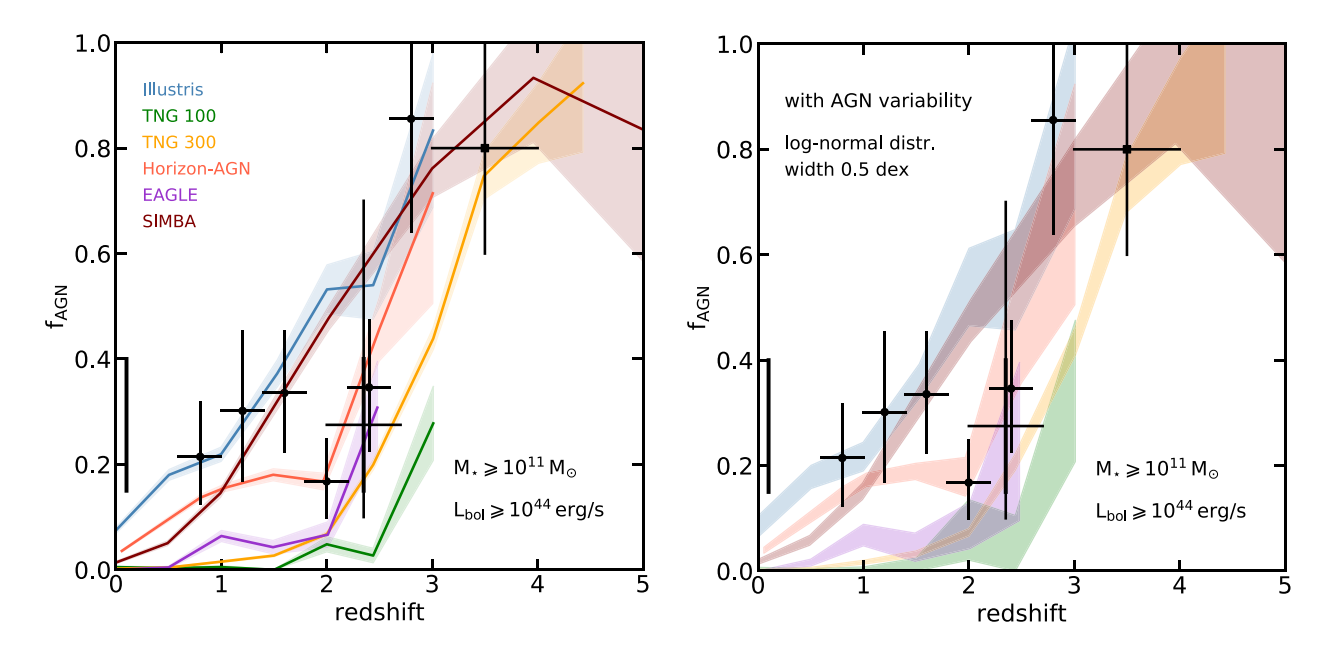


Figure 9. Left-hand panel: Fraction of AGN with $L_{bol} \ge 10^{44}$ erg s⁻¹ in massive galaxies of $M_{\star} \ge 10^{11}$ M_☉ (right-hand panels). Only redshift bins with more than 10 galaxies are included. The regime of massive galaxies is important as we expect that a large fraction of these galaxies should be quiescent. We show in black existing observational constraints for this regime of massive galaxies (Kauffmann et al. 2003; Kriek et al. 2007; Cowley et al. 2016; Marsan et al. 2017). At high redshift, all the simulations have a large fraction of AGN in massive galaxies, in agreement with observations. However, at lower redshift ($z \le 2$) there is a plateau in observations at 20–40 per cent of the galaxies hosting an AGN, which is not well reproduced in some of the simulations. Right-hand panel: Effect of AGN variability with a lognormal distribution of width 0.5 dex. Shaded regions show the minimum and maximum values of the 15th–85th percentiles of the AGN fraction distributions over several realizations of our AGN variability model.

The increase of the AGN fraction at $z\sim0$ that we find in all simulations between galaxies with $M_{\star}\sim10^9\,{\rm M}_{\odot}$ and those with $M_{\star}\sim10^{10}\,{\rm M}_{\odot}$ was also found in observations (Man et al. 2019). The increase with galaxy stellar mass in the low-redshift Universe was also found in Aird et al. (2012).

5.2 AGN fraction in massive galaxies

The number of AGNs in massive galaxies through cosmic time is crucial for assessing the role of AGN feedback in these galaxies. Observational constraints are based on relatively poor number statistics (Kriek et al. 2007; Cowley et al. 2016; Marsan et al. 2017), with samples including 10 or fewer galaxies of $M_{\star} \ge 10^{11} \,\mathrm{M}_{\odot}$, but they provide us with a first insight into the fraction of AGN in massive galaxies up to $z \sim 3.5$. The sample of Marsan et al. (2017) finds an AGN fraction of \geqslant 80 per cent with $L_{\rm bol} \sim 10^{44}$ – 10^{46} erg s⁻¹ in six galaxies $(M_{\star} \sim 1.5 - 4 \times 10^{11} \,\mathrm{M}_{\odot}, 3 < z < 4)$. Cowley et al. (2016) also find that ≥80 per cent of their galaxy sample from zFOURGE hosts an AGN in the range of 2.6 < z < 3.2. At lower redshift, Kriek et al. (2007) study a sample of 11 galaxies $(M_{\star} \sim 3 \times 10^{11} \,\mathrm{M_{\odot}}, \, 2 < z < 2.7)$ with some of them hosting an AGN of $L_{\rm bol} \sim 10^{44}\,{\rm erg\,s^{-1}}$ or evidence for narrow-line emission, and therefore, find an AGN fraction of ~20 per cent. We also report the estimates of \sim 20-40 per cent of Cowley et al. (2016) at lower redshifts $(0.5 \le z \le 2.5)$. We reproduced all these different constraints as black crosses in Fig. 9. About 80 per cent of the massive galaxies host an AGN at high redshift ($z \ge 2.5$). At z < 2.5, the observational constraints on the fraction of AGN vary in the range of 20-40 per cent (SDSS data; Kauffmann et al. 2003).

We show in Fig. 9 the fraction of simulated AGN with $L_{\rm bol} \ge 10^{44}\,{\rm erg\,s^{-1}}$ in massive galaxies of $M_{\star} \ge 10^{11}\,{\rm M}_{\odot}$. Simulations of $\sim 100\,{\rm cMpc}$ side length start forming galaxies of $\sim 10^{11}\,{\rm M}_{\odot}$ only at z

 \sim 3–4. The simulation TNG300 (and SIMBA) with its larger volume allows us to investigate the fraction of AGN in massive galaxies at much earlier times (Habouzit et al. 2019). We find the same overall trend in all the simulations: A high fraction of massive galaxies host an AGN at high redshift, and the fraction decreases towards lower redshift. While this trend is in good agreement with the observations, the AGN fractions found in simulations can vary substantially. The difference in the fractions for the Illustris and TNG simulations reaches up to 50 per cent in the redshift range z = 3-2, for example. In general, we see here that in the simulations there is no consensus on the possible sharp decrease of the AGN fraction at $z \sim 2.5$ found in the observations. There is also no consensus on the fraction of AGN found in these massive galaxies, even at relatively low redshifts $z \le$ 2. Some of the simulations produce very low fractions of AGN for these redshifts, which could indicate a too efficient self-regulation of these BHs by their AGN feedback.

The AGN fractions strongly depend on the model that we use to compute the AGN bolometric luminosity, i.e. whether we assume that all AGNs are radiatively efficient or not, as well as on the radiative efficiency $\epsilon_{\rm r}$. To illustrate this, we show in Fig. A2 the same Fig. 9 but assuming the same radiative efficiency of $\epsilon_{\rm r}=0.1$ for all the simulations, instead of $\epsilon_{\rm r}=0.2$ and that all AGNs are radiatively efficient (as assumed in many analyses of simulations, but however disfavoured by observations in massive galaxies whose BHs often lie in the range $f_{\rm Edd}=0.01$ –0.1; Russell et al. 2013). The latter results in an enhancement of the fraction of AGN in all the simulations, leading to a better agreement with observations for z<2.

We show in Fig. 9 (right-hand panel) the impact of AGN variability on the fraction of AGN in massive galaxies. AGN variability broadens the range of possible values of the AGN fraction, including at z < 1 when several simulations have very low fractions, but does not affect the conclusions of this section.

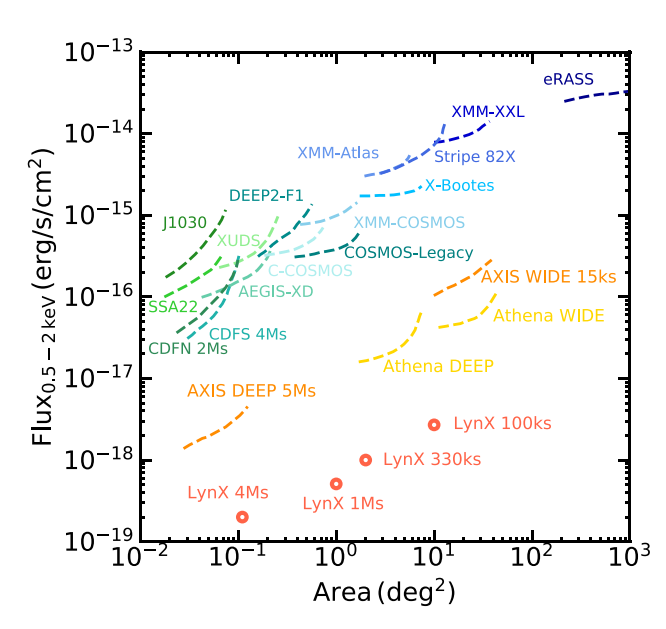


Figure 10. Sensitivity curves of current X-ray missions (green to blue colours). For all surveys, the curves represent the sensitivity within the 20–80 per cent total survey area. We show the curve of the new Athena mission in yellow, and of the AXIS and LynX concept missions in orange and red, respectively.

6 PREDICTIONS FOR UPCOMING OR PLANNED X-RAY MISSIONS

In this section, we predict the number of AGNs from the six large-scale cosmological simulations that would be detectable by the upcoming Athena mission (Nandra et al. 2013) and the AXIS (Marchesi et al. 2020, and references therein) and LynX (The Lynx Team 2018) planned missions. In the previous sections, we showed that the different simulations all predict different populations of AGNs, not always in perfect agreement with current observational constraints. However, the predictions that we derive below are important as they cover the broad range of subgrid modelling (BH seeding, accretion, feedback, and galaxy physics) employed in simulations.

6.1 The landscape of X-ray surveys, and AGN detection in new X-ray missions

Athena, AXIS, and LynX all have different luminosity thresholds to detect AGNs. Their sensitivity curves express the flux that can be reached by the observations of a given instrument as a function of the sky area covered by the survey. We show the 0.5–2 keV sensitivity curves of Athena, AXIS (Marchesi et al. 2020), and LynX (private communication with Alexey Vikhlinin and Niel Brandt) in Fig. 10. Athena, AXIS, and LynX will/would increase by one order of magnitude the sensitivity in the X-ray band at fixed area compared to previous surveys⁸ (in Fig. 10, green to blue colours). The sensitivity of a given survey depends on its exposure time and size. At fixed parameters, the sensitivity of LynX should be more than 3 times better than the sensitivity of AXIS. Indeed, while having the same telescope design, the AXIS effective area is 3.3 times smaller than LynX.

Table 1. Characteristics of several surveys for Athena, AXIS, and LynX: covered area, flux sensitivity (0.5–2 keV band) that could be reached, and exposure time.

Surveys	Area (deg ²)	$F ({\rm erg}{\rm s}^{-1}{\rm cm}^{-2})$	Exposure
Athena DEEP	5.28	$(1.6-6.5) \times 10^{-17}$	1 Ms
Athena WIDE	47.52	$(4.2-11) \times 10^{-17}$	90 ks
LynX DEEP	0.11	$2.0 \times 10^{-19} 2.0 \times 10^{-18}$	4 Ms
LynX WIDE	10		100 ks
AXIS DEEP	0.16	$(1.4-4.5) \times 10^{-18}$	5 Ms
AXIS WIDE	50	$(1.0-2.8) \times 10^{-16}$	15 ks

To predict the population of AGN that could be detected by Athena, AXIS, and LynX, we define several possible surveys. All have been already discussed by the different mission teams and/or in the literature. The parameters of these surveys are all different (i.e. in terms of survey size, exposure time, and sensitivity), and thus, our predictions for the missions below cannot be compared with one another. Predictions for any other survey parameters are available upon request. We use two different surveys for Athena, as described in Nandra et al. (2013), two possible surveys for LynX (private communication with LynX researchers), and we follow the papers of Mushotzky et al. (2019) and Marchesi et al. (2020) to define two surveys for AXIS. We report the parameters of these surveys in Table 1. We convert the 0.5-2 keV sensitivity curves into 2-10 keV luminosity detection limits, as explained in Appendix B1. In general, LynX should detect AGNs fainter by one order of magnitude than AXIS, at all redshifts. The WIDE field of AXIS could reach a similar sensitivity of the WIDE survey of Athena, but for reduced exposure time (e.g. 15 ks instead of 90 ks).

6.2 Predictions for the number of detectable AGNs for the different simulations

We show the number of detectable AGNs $N_{\rm AGN}$ in a volume of $(100\,{\rm cMpc})^3$ in Fig. 11 (top panel), for all the surveys described in Table 1. We also provide similar predictions but presented as $N_{\rm AGN}/{\rm dz}/{\rm d\Omega_{\rm survey}}$ in Fig. 11 (bottom panel), i.e. the number of detectable AGNs per slice of redshift and for the field of view of the different surveys. The shaded regions bracket, for each simulation, the number of detections when corrected for obscured AGN with our second AGN luminosity- and redshift-dependent obscuration model (see Fig. 1). With this model, we either remove the AGN from the samples (lower edges of the shaded regions in Fig. 11) or we decrease their hard X-ray luminosity by one order of magnitude (upper limits). Other models are tested in Appendix B2. We specify here that the impact of obscuration in the observed 0.5–2 keV band is redshift dependent, and also that the missions will have 2–10 keV sensitivity, which is less affected by obscuration.

We provide in Table B1 the best fit for the number density of AGN per (100 cMpc)³ shown in Fig. 11 for the second AGN luminosity-and redshift-dependent obscuration model. These best fits can be used to prepare the future X-ray missions, i.e. to bracket how many AGNs could be detected, and investigate the optimal size of the mission surveys.

The number density of detections varies strongly from one simulation to another. At $z \ge 5$, the fewest AGNs would be detected in Horizon-AGN and SIMBA, with between 20 and 150 detections per $(100 \text{ cMpc})^3$ at the sensitivity of the LynX Deep and Wide surveys, about 20–80 for the AXIS Deep and Wide surveys, and from less than 10–40 for Athena surveys. Illustris and TNG100 predict more AGNs

⁸The sensitivity curves for previous X-ray missions are taken from Civano et al. (2016) and Marchesi et al. (2020).

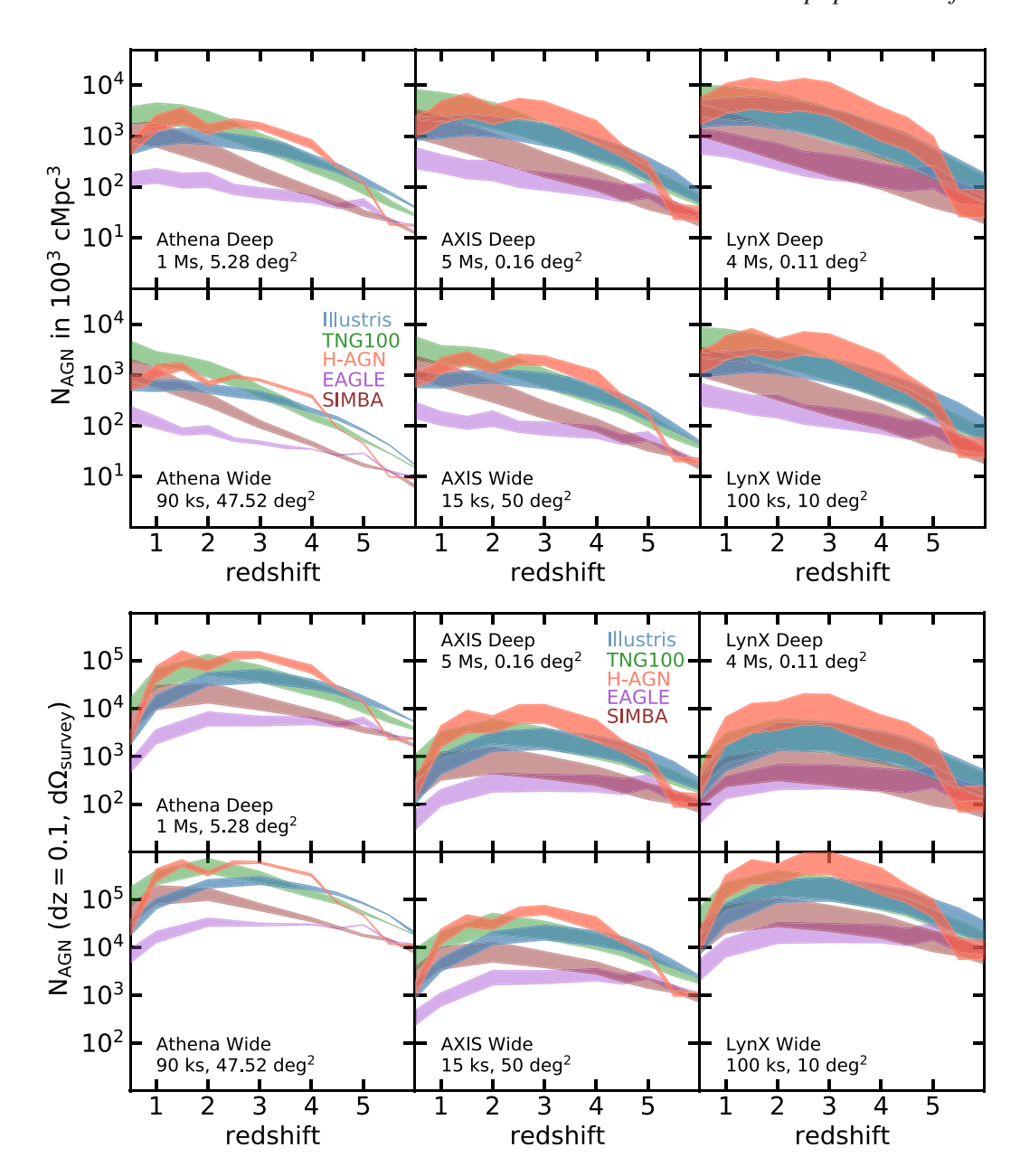


Figure 11. Top panel: Number of AGN detections per $(100\,\text{cMpc})^3$ in galaxies of $M_\star\geqslant 10^9\,\text{M}_\odot$ for the sensitivity of a couple of possible Athena, AXIS, and LynX surveys. The numbers of AGNs are not comparable between the different surveys, as we show different exposure times and sizes of surveys. The shaded areas bracket the number of detections per $(100\,\text{cMpc})^3$ when corrected for obscured AGN (our second AGN luminosity- and redshift-dependent model), when we remove the AGN (lower edge of the shaded region), and when we decrease their luminosity (upper edge). The simulations predict different numbers of detectable AGNs. At low redshift (z < 2), EAGLE predicts a number of AGNs one order of magnitude lower than the other simulations. At high redshift (z > 4), Illustris and TNG100 predict more AGNs than the other simulations. Bottom panel: Number of detectable AGNs in the field of view of the given Athena, AXIS, and LynX surveys, and for redshift slices of dz = 0.1.

to be detected at the same redshifts, with e.g. 140–180 detections per $(100\,\mathrm{cMpc})^3$ with LynX Deep and Wide surveys, 50-90 with AXIS surveys, and 20–40 with the Athena surveys. The number of AGNs that could be detected increases with decreasing redshift until $z\sim2$, at which point the number of AGNs stabilizes or decreases (e.g. for Horizon-AGN, Illustris). At z=1, we find more similar predictions for the total number of AGNs detectable with the missions for Horizon-AGN, Illustris, and SIMBA. TNG100 is the simulation predicting the highest number of AGNs to be uncovered.

When considering the entire AGN population, independently of their BH mass or galaxy stellar mass, the Athena, AXIS, and LynX missions will be able to constrain the AGN population produced by cosmological simulations. More precisely, there is more than an order magnitude of difference in the number of detectable AGNs in the different simulations. Thus, being able to detect fainter AGNs in new surveys will be crucial to discriminate between simulation subgrid models. The shape of the number of detections with redshift also varies from one simulation to another, and it could also be used to constrain the modelling. Depending on the simulated population of AGNs, the impact of obscuration can sometimes be significant (large shaded areas in Fig. 11). This is a large source of uncertainty when comparing simulations to observations, and unfortunately

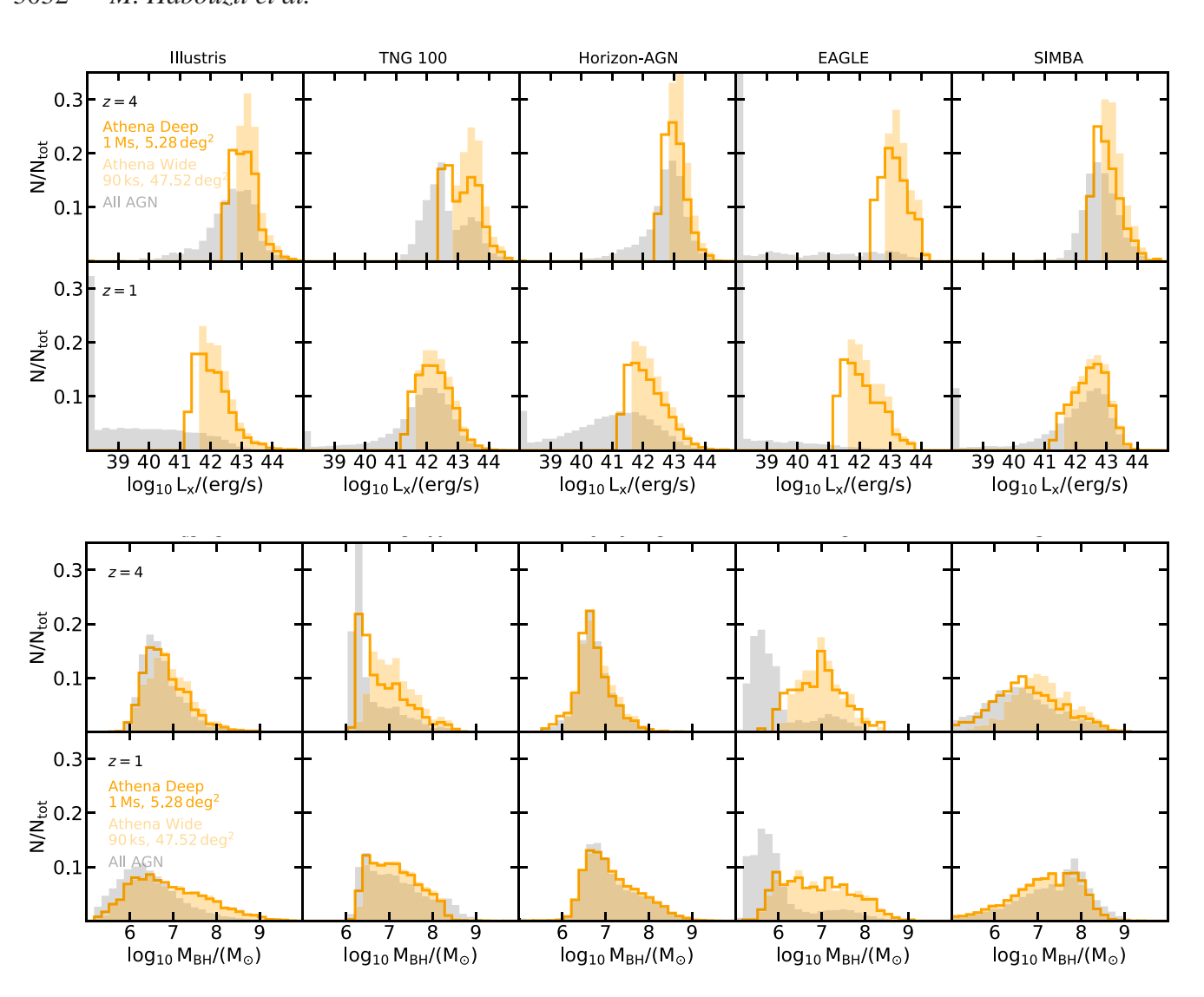


Figure 12. Athena deep (1 Ms of exposure time, 5.28 deg²) and wide (90 ks, 47.52 deg²) surveys. Top panels; Normalized distributions of the hard (2–10 keV) X-ray luminosity of the AGNs that are detectable. For reference, we show in grey the distribution of all the AGNs with $L_x \ge 10^{38}$ erg s⁻¹ in the simulations. Bottom panels: Normalized distributions of BH mass corresponding to the detectable AGN. We only include galaxies with $M_{\star} \ge 10^9 \, \mathrm{M}_{\odot}$ in all the panels.

obscuration and the intrinsic number of AGN produced by the simulations are degenerate.

6.3 Populations of AGN and BHs to be uncovered by the new X-ray observatories

The sensitivity of Athena, AXIS, and LynX being different, these missions will have access to different populations of AGNs and BHs, as shown in Figs 12, 13 and 14. These figures show the distributions of AGN hard X-ray luminosity of the detectable AGN, and the corresponding BH mass distributions (although not measurable by the X-ray missions) for z = 4 and 1. Deep surveys (higher sensitivity) are shown with the darkest colour, and the wide surveys (lower sensitivity) with the lightest colour and shaded histograms. For reference, we show in grey in all the panels the distribution of the intrinsic AGN population produced by the simulations. The sensitivity of the Athena wide survey of 50 deg² will capture AGN with $L_x \ge 10^{43} \text{ erg s}^{-1}$ at high redshift, and AGN with $L_x \ge 10^{42} \, \mathrm{erg \, s^{-1}}$ at low redshift. In the TNG100 simulation at z = 4, Athena would see the peak of the L_x luminosity distribution

corresponding to the efficient accretors, which are mostly powered by $\leq 10^8 \,\mathrm{M}_{\odot}$ BHs in TNG100. However, the Athena wide survey would not detect any AGN of the fainter peak of the luminosity distribution. In TNG100, these AGNs are powered by massive BHs with $M_{\rm BH} \geqslant {\rm a \, few \, 10^8 \, M_{\odot}}$ entering in the kinetic mode of AGN feedback, and responsible for regulating themselves (see bimodality in the Eddington ratio distribution of TNG100, Fig. 3) and quenching their host galaxies. In EAGLE, a significant population of the BHs are not efficient accretors, and have low luminosities. While Athena will go deeper than the current X-ray missions, it will be insufficient to detect most of the AGN population in EAGLE (see the mismatch of the grey and yellow L_x and $M_{\rm BH}$ distributions in Fig. 12). The mission would see the AGN powered by BHs of $M_{\rm BH} \sim 10^{6-8.5}\,{\rm M}_{\odot}$ at z = 4, but not the lower mass BHs that constitute most of the BH population in EAGLE. In some simulations such as TNG100, the Athena deep survey will start uncovering the faint regime of the AGN, and provide us with a distribution of BH masses more similar to the intrinsic distribution produced by the simulations. However, it will not be sufficient to access the full spectrum of the AGN population.

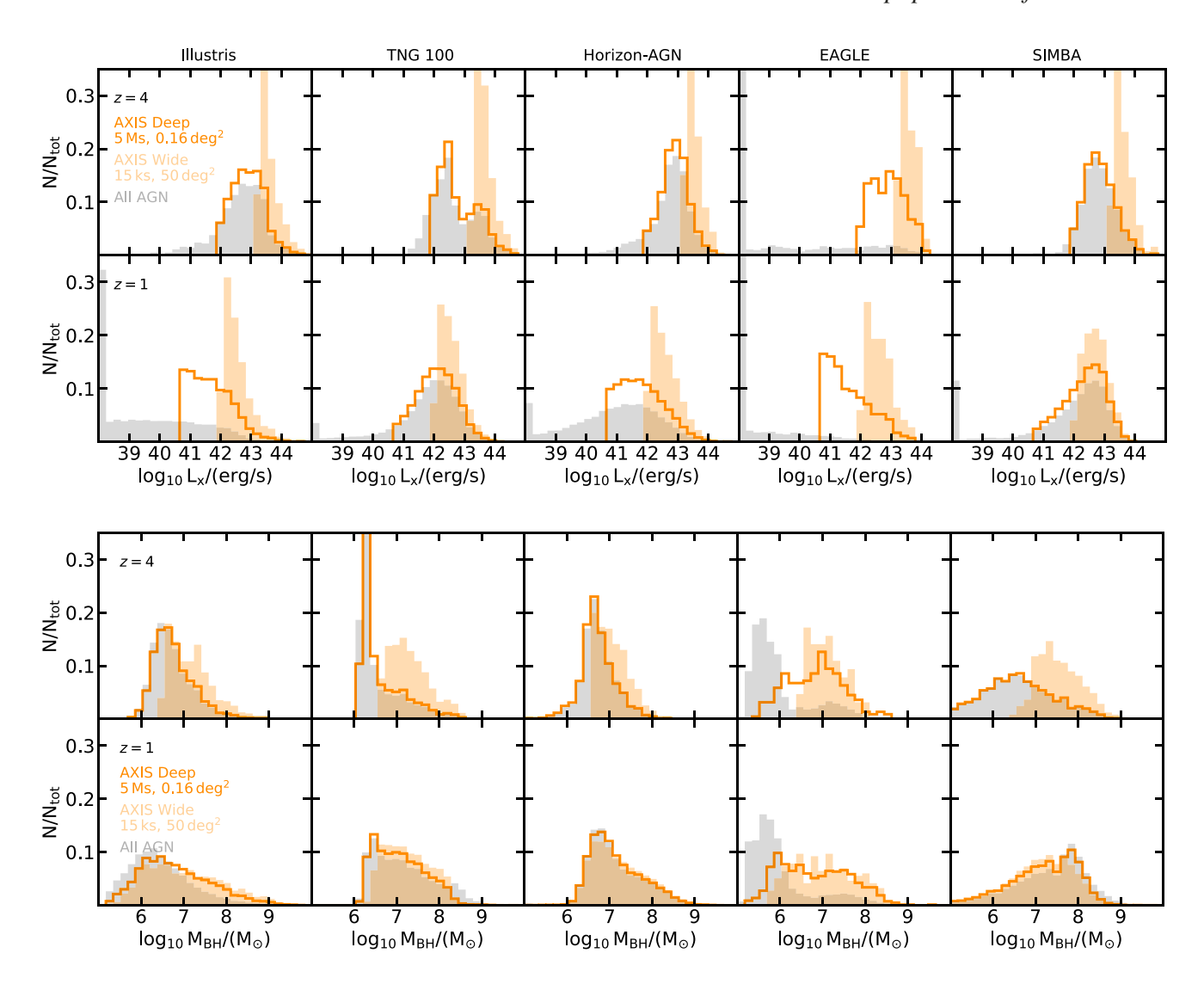


Figure 13. AXIS deep (5 Ms of exposure time, 0.16 deg^2) and wide (15 ks, 50 deg^2) surveys. Top panels: Normalized distributions of the hard (2–10 keV) X-ray luminosity of the AGNs that are detectable. Distribution of all the AGNs with $L_x \ge 10^{38} \text{ erg s}^{-1}$ is shown in grey. Bottom panels: Normalized distributions of BH mass corresponding to the detectable AGN. Only $\ge 10^9 \text{ M}_{\odot}$ galaxies are included.

The AXIS mission will have a higher sensitivity than Athena. We find that the AXIS wide survey and the Athena deep survey (as we defined them) provide similar results. Now, looking at the deep AXIS survey in Fig. 13, we see that in theory it would provide us with distributions of $L_{\rm x}$ and $M_{\rm BH}$ very consistent with the simulation intrinsic distributions. If the Universe hosts an AGN population similar to the EAGLE simulation, i.e. with globally fainter AGN than the other simulations, we would still miss a significant fraction of the AGN population with such a deep AXIS survey.

LynX will have the highest sensitivity, orders of magnitude better than the current X-ray facilities, and about one order of magnitude higher than Athena. In Fig. 14, we find that the LynX mission will indeed probe much fainter AGNs, with e.g. $L_x \geq 10^{41.5}\,\mathrm{erg\,s^{-1}}$ at z=4, and $L_x \geq 10^{40.5}\,\mathrm{erg\,s^{-1}}$ at z=1, for the wide survey that we defined. The deep survey should access even fainter AGNs, with e.g. $L_x \geq 10^{40.5}\,\mathrm{erg\,s^{-1}}$ at z=4, and $L_x \geq 10^{39}\,\mathrm{erg\,s^{-1}}$ at z=1. We find that with LynX the distributions of AGN luminosities (and corresponding BH masses) would be representative of the intrinsic simulated population of BHs, except for EAGLE. The observed distribution at high redshift would highlight a relatively

more significant population of massive BHs while in reality the population of lower mass BHs would be larger in EAGLE.

6.4 Will small fields of view allow for enough detections?

In Figs 12, 13, and 14, we showed the $L_{\rm x}$ and $M_{\rm BH}$ distributions that could be accessible by the different surveys (simply selecting all AGNs with $L_{\rm x} \geqslant L_{\rm limit\, survey}$). The number of AGN detections depends on the size of the surveys, and for a very small field of view if for example only 10 AGNs are detected, the obtained distributions would not be representative of the intrinsic distributions. To investigate this, we randomly select from our samples the number of AGNs that would be observable for the different surveys (as shown in Fig. 11), i.e. for their fields of view $\Omega_{\rm survey}$, given redshift slices, and including the effect of obscuration. We test three different redshift slices of dz = 0.1, 0.01, and 0.001. dz = 0.1 represents the uncertainty of redshift estimate of the host galaxies at high redshift, and the two other dz are purposely smaller to be conservative. Measuring redshifts with an uncertainty of dz = 0.01 is difficult but possible.

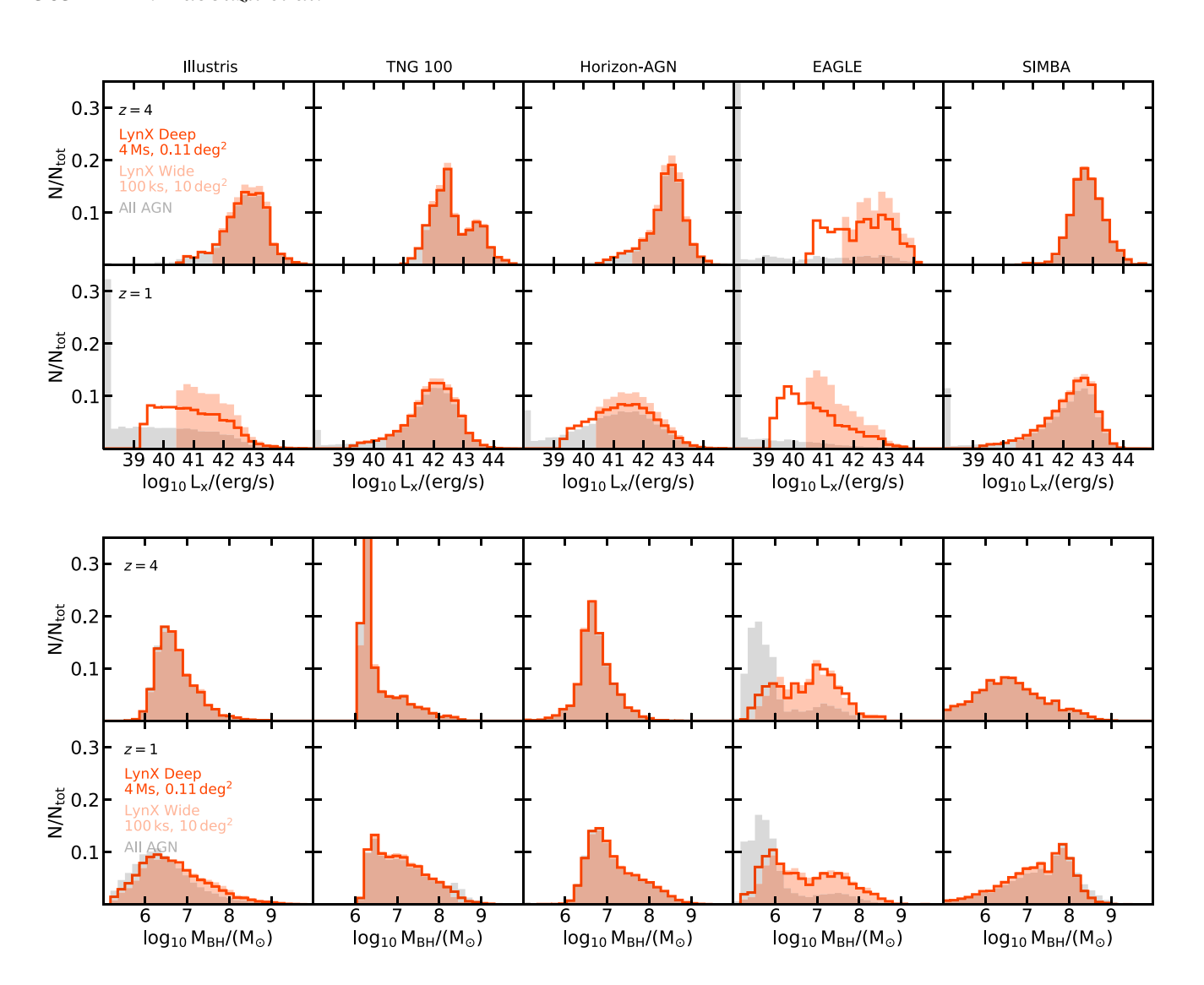


Figure 14. LynX deep (4 Ms of exposure time, 0.11 deg²) and wide (100 ks, 10 deg²) surveys. Top panels: Normalized distributions of the hard (2–10 keV) X-ray luminosity of the AGNs that are detectable. Distribution of all the AGNs with $L_x \ge 10^{38}$ erg s⁻¹ is shown in grey. Bottom panels: Normalized distributions of BH mass corresponding to the detectable AGN. Only $\ge 10^9$ M_{\odot} galaxies are included. The high sensitivity of LynX could make accessible almost the full L_x and $M_{\rm BH}$ distributions predicted by the Illustris, TNG100, Horizon-AGN, and SIMBA simulations. At $z \le 1$, there are more and more quiescent BHs with $L_x < L_{x, LynX}$ that will be missed. In EAGLE, the L_x and $M_{\rm BH}$ distributions that could be obtained with LynX (even with a very large survey) would still not have the same shape as the EAGLE BH population. This is because of the significant number of faint and quiescent AGNs at all times in EAGLE.

Redshift accuracy of dz = 0.001 will be extremely difficult for a large number of sources, especially for faint objects.

For all the wide Athena, AXIS, and LynX surveys used here, and for $\mathrm{d}z=0.01$ and z=1–4, there would be enough AGN detections in the survey's Ω_{survey} to recover the L_{x} and M_{BH} distributions, for all the simulations. This is with the exception of EAGLE at low redshift, e.g. z=1, for which the low number of detections may not allow us to completely recover the shape of the intrinsic L_{x} distribution for the small slices of redshifts.

The intrinsic L_x distributions of the simulations can also be recovered for the deep field surveys, which have small fields of view, in large redshift slices of dz = 0.1 and 0.01. More precisely, we find that the deep field of Athena (5.28 deg²) provides a sufficient number of detections to recover the intrinsic distributions even for dz = 0.001. For the AXIS deep survey, the L_x and $M_{\rm BH}$ distributions can be recovered for $dz \geq 0.01$ for all the simulations except

EAGLE. We find similar results for the deep field of LynX. We show the impact of a deep survey of $0.11 \, \text{deg}^2$ LynX in Fig. 15 with in black the distributions that we would get from the actual detections of the survey. In the case of dz = 0.001, i.e. if very high precision is obtained for the host galaxy redshift, it will be difficult to recover the intrinsic distributions predicted by any of the simulations at a given redshift with the few detections (see Fig. 15, bottom panels).

In general, these new upcoming and concept missions will have the power to provide us with a unique view of the distribution of BHs, because they will be able to observe fainter AGNs than current X-ray facilities. If the surveys cover a sufficiently large field of view, they will probe BH populations that we could compare with results from cosmological simulations. Some of the simulations have sufficiently different distributions of AGN luminosity that we could be able to constrain subgrid models of BH physics.

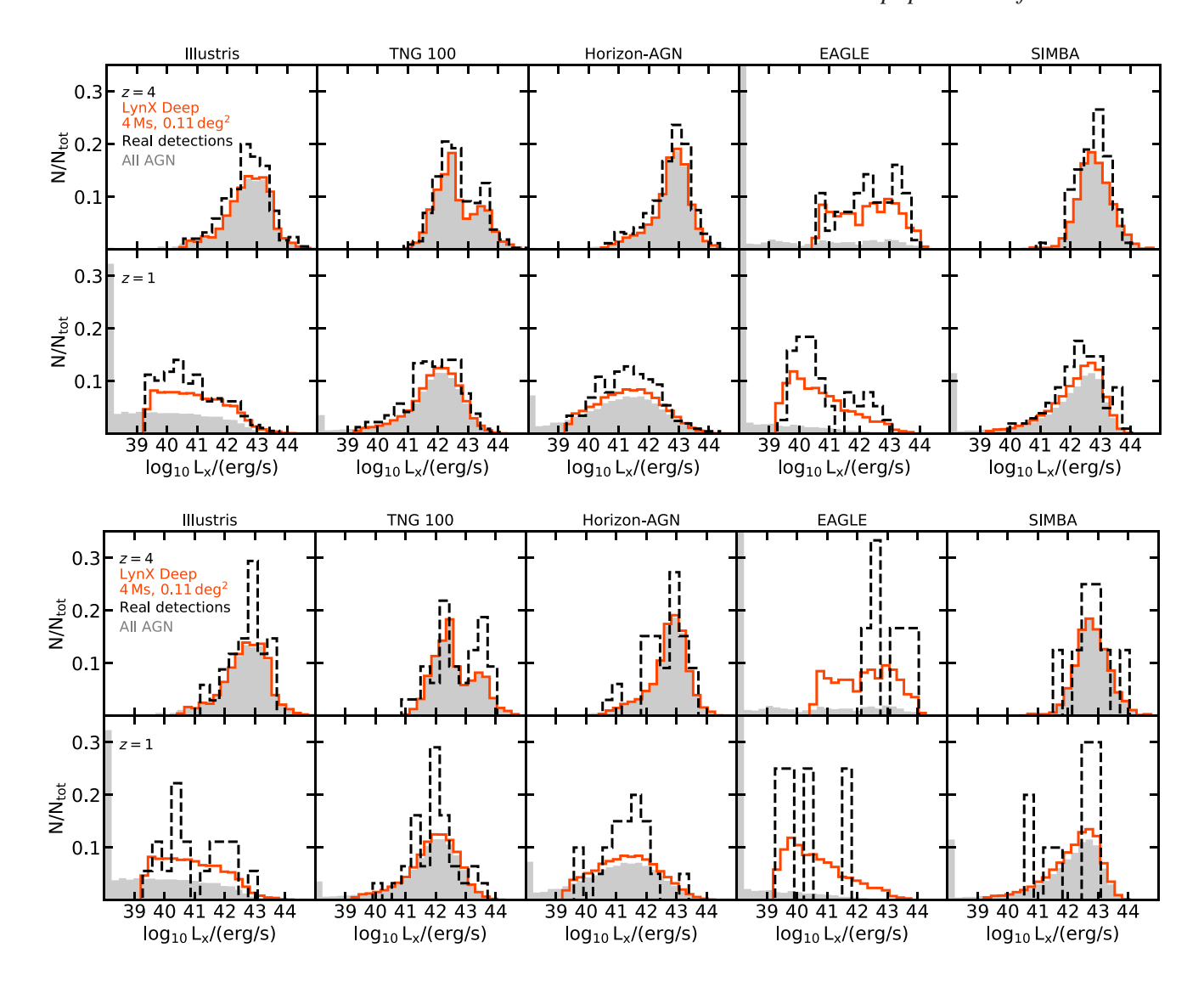


Figure 15. Illustration of how small fields of view would affect our understanding of the AGN L_x distribution. We show in grey the intrinsic AGN population produced by simulations, and in red the population that could be detected by the deep survey of LynX (simply assuming $L_{AGN} \ge L_{\text{limit, survey}}$) in each simulation. In black, we show how the distributions would look like with the real number of AGN detections in a deep field of view of the LynX mission, assuming a redshift accuracy of either dz = 0.01 (top panels) or dz = 0.001 (bottom panels).

7 DISCUSSION

7.1 Interpretation of the differences between the number of AGNs in simulations and in observations

Throughout this paper, we have demonstrated that some simulations overproduce, while some underestimate, the number of AGNs with respect to observational constraints, particularly for $z \geq 1$. Combining all the diagnostics from this paper, i.e. the AGN luminosity function (Fig. 5), the Eddington ratio distribution for different BH mass bins (Fig. 3), and the fraction of AGN in massive galaxies (Fig. 9), to the diagnostics studied in Habouzit et al. (2020), i.e. the $M_{\rm BH}-M_{\star}$ diagram and the BH mass function, we can now explain the causes of such differences with observations. We caution here that our interpretation relies on the accuracy of the observational constraints, and that we would need to review it as new constraints become available.

7.1.1 Simulation with a lower luminosity function than current observational constraints

The AGN population produced in EAGLE is generally in better agreement with current observational constraints than the other simulations. However, we find a lower luminosity function than the constraints in the bright regime, i.e. for $L_{\rm x} \geqslant 10^{44}\,{\rm erg\,s^{-1}}$ (Fig. 5). The lower luminosity function likely comes from a lower fraction of AGN powered by relatively massive BHs of $M_{\rm BH} \sim 10^8-10^9\,{\rm M}_{\odot}$. This is shown by the lower BH mass function for this regime with respect to observational constraints (see fig. 11 of Habouzit et al. 2020), but also by the absence of BHs with Eddington ratios $f_{\rm Edd} > -2$ for BHs of $M_{\rm BH} \sim 10^8-10^9\,{\rm M}_{\odot}$ (Fig. 3). Compared to the other simulations, there are fewer BHs in this mass range, and they are not accreting at high accretion rates. The smaller accretion rates result from the combination of the strong SN feedback, AGN feedback, and the modified Bondi accretion model of EAGLE that takes into account angular momentum (Rosas-Guevara et al. 2015).

7.1.2 Simulations with a higher luminosity function than current observational constraints

In simulations such as Horizon-AGN and Illustris, weak SN feedback could be responsible for the larger number of AGNs in relatively lowmass galaxies with $M_{\star} \leq 10^{10} \, \mathrm{M}_{\odot}$ compared to observations. Excluding the least massive galaxies from the AGN luminosity function, for example by applying a cut of $M_{\star} \ge 10^{9.5} \,\mathrm{M}_{\odot}$ (see also Volonteri et al. 2016), leads to a lower normalization of the AGN luminosity function and better agreement with current observational constraints. This could indicate that a large fraction of the AGNs located in the low-mass galaxies are not sufficiently regulated by SN feedback. This can be connected to the galaxy mass functions produced by simulations and their agreement with observational constraints. The SN feedback model of Illustris (Vogelsberger et al. 2014a) has been modified in the TNG simulations to correct for the larger stellar mass function in the low-mass regime (see fig. 4 in Pillepich et al. 2018, for a comparison between the Illustris and TNG models). The TNG simulations also overproduce the AGN luminosity function. The high number of AGNs could be explained by the fast-growing BHs with $M_{\rm BH} \leqslant 10^8\,{\rm M}_\odot$ in galaxies of $M_\star=10^{10}$ – $10^{10.5}\,{\rm M}_\odot$. These fastgrowing BHs are found just after the regime where BHs and galaxies are regulated by SN feedback and before the regime where AGNs are regulated by AGN feedback. Indeed, we find that the Eddington ratio distributions of the TNG BHs with $M_{\rm BH} \leq 10^8 \, \rm M_{\odot}$ peak at higher $f_{\rm Edd}$ than in the observational constraints available at z=0 (Fig. 3). Since the ratios are proportional to $\dot{M}_{\rm BH}/M_{\rm BH}$, the higher ratios indicate too high accretion rates for the given mass of the BHs. We can also connect this to the higher normalization of the TNG100 BH mass function for $M_{\rm BH} \leq 10^8 \, \rm M_{\odot}$ (fig. 11 of Habouzit et al. 2020). Interestingly, we note better agreement of the BH mass function for TNG300 with observations, and also better agreement of the AGN luminosity function of TNG300. SIMBA is an interesting case: This simulation produces a BH mass function not too different from the EAGLE mass function for $M_{\rm BH} \leqslant 10^{8.5}\,{\rm M}_{\odot}$ at z>1 (see fig. 11 of Habouzit et al. 2020), and in agreement with observations, but produces an AGN luminosity function with a higher normalization than EAGLE. From the Eddington ratio distributions shown in Fig. 3, the main difference between SIMBA and EAGLE is the ability (and number) of BHs with $M_{\rm BH} \geqslant 10^7 \, \rm M_{\odot}$ to accrete efficiently and to power a large number of bright AGNs with $L_{\rm bol} \ge 10^{45} \, \rm erg \, s^{-1}$ (see fig. 2 of Habouzit et al. 2020). Our results highlight that different populations of BHs can be responsible for the higher normalization of the AGN luminosity functions produced in simulations compared to the current observational constraints.

7.2 Moving forward: how to discriminate between simulation models with observations

In this paper, we have investigated the properties of the AGN populations produced by large-scale cosmological simulations. With various diagnostics (e.g. Eddington ratio distribution, AGN luminosity function, and fraction of galaxies hosting an AGN), we showed that the simulations studied here do not reach a consensus on the population of AGNs that they form. Given that none of the simulations was calibrated on AGN properties, their agreement with current observations is reasonable in some regimes, but still need to be worked on in some other regimes, as explained below. Some observational constraints also carry large uncertainties, e.g. at high redshift (e.g. AGN fraction in massive high-redshift galaxies and number density of faint AGN at $z \ge 4$), which makes the improvement of cosmological simulations a difficult task.

One major difference among the simulations is the population of relatively faint AGNs with $L_x \sim 10^{42-44} \, \mathrm{erg \, s^{-1}}$ at $z \geq 1$. Indeed, the AGN luminosity function of different simulations can vary by more than one order of magnitude for, e.g. $L_x \sim 10^{43} \, {\rm erg \, s^{-1}}$ (Figs 5 and 7). Moreover, the population of faint AGNs is powered by different BHs (and hosted in different galaxies) in the simulations. In TNG100 and SIMBA, the population of faint AGNs is significantly driven by massive BHs in massive quiescent galaxies, while in other simulations such as Illustris and EAGLE, the faint AGNs are powered by lower mass BHs in relatively low-mass galaxies (Schirra et al. 2021). The distinction of these populations in Horizon-AGN is not as strong, and faint AGNs are powered by the two populations. We find (Fig. 7) that the large discrepancies between simulations and observations in the number of faint AGNs could arise from simulations producing too many of these faint AGNs in low-mass galaxies of $M_{\star} = 10^9 \text{--} 10^{10} \,\mathrm{M}_{\odot}$ at $z \geq 1$, compared to observations where most AGNs are found in galaxies of $M_{\star} \ge 10^{10} \,\mathrm{M}_{\odot}$. In observations, there is a good agreement among studies for the space density of bright AGNs with $L_x \ge 10^{43} \, \mathrm{erg \, s^{-1}}$ for $z \ge 1$ (e.g. Brusa et al. 2009; Civano et al. 2011), but the regime of faint AGNs with $L_{\rm x} \sim 10^{42} - 10^{43} \, {\rm erg \, s^{-1}}$ has larger uncertainties, and even more for higher redshift (e.g. Ueda et al. 2014; Aird et al. 2015; Buchner et al. 2015; Giallongo et al. 2015, and our Fig. 7). A source of uncertainty could be the fraction of heavily obscured Compton-thick AGN. We note that recent studies have investigated the fraction of obscured and unobscured AGNs up to high redshift of $z \sim 4-5$ (e.g. La Franca et al. 2005; Aird et al. 2015; Marchesi et al. 2016; Ricci et al. 2017; Ananna et al. 2020, and references therein). This regime needs to be exploited to constrain further the subgrid models of the simulations, here likely the models of accretion and of AGN feedback. While there is a diversity of AGN feedback implementations, most simulations (except SIMBA) employ variations of the Bondi model. Because the uncertainties on accretion processes are large, and accretion modelling can strongly impact the AGN populations, our work motivates the needs to explore more models. Today, exploring the faint regime is very challenging given the current X-ray facilities, but should become achievable with the Athena mission to be launched in ~2030 and the AXIS and LynX concept missions. Measuring the redshift of the AGN host galaxies could be possible, e.g. with 30 m telescopes, allowing us to understand the co-evolution of the faint AGNs and their galaxies. Both observations and simulations/theory will benefit from new high-sensitivity X-ray surveys.

Observationally, moving to the faint regime will be challenging as the contribution from X-ray binaries (XRBs) to the galaxy total X-ray emission is still unknown. XRBs could contribute significantly as shown in both observations (e.g. Fornasini et al. 2018; Lehmer et al. 2019) and simulations (Schirra et al. 2021). In the latter, the XRB contribution is estimated as a function of galaxy mass and SFR. These quantities both differ from one simulation to another, leading to strong discrepancies in the XRB contribution among simulations (Schirra et al. 2021).

In this paper, we also find that the fraction of galaxies hosting an AGN varies strongly from one simulation to another, and this could open a new path to constrain simulation subgrid physics. This is interesting at both low and high redshifts, and in both low- and high-mass galaxies, for different reasons. The fraction of massive quenched galaxies produced at $z \le 3$ differs in all the simulations, but is in good agreement with observational constraints at first order (e.g. Schaye et al. 2015; Kaviraj et al. 2019; Donnari et al. 2019, 2020). AGNs are responsible for quenching massive galaxies in these simulations, and as we have demonstrated in this paper the AGNs do not have the same properties in all the simulations. The

population of AGNs needs to be investigated in more detail and compared to observations. To understand the cosmic evolution of the Universe, galaxy formation, and the co-evolution between BHs and galaxies, large-scale cosmological simulations need to reproduce both the population of galaxies and the population of BHs and AGNs. From Fig. 9, several simulations appear to lack AGN in massive galaxies at $z \le 2$ (when using the radiative efficiency ϵ_r used in the simulations) when compared to observational constraints. Therefore, AGN feedback in simulations could be efficient enough to quench as many massive galaxies as observed, but somehow too efficient in regulating the AGN themselves. This paradox needs to be addressed.

In observations, the fraction of massive galaxies with $M_{\star} \ge 10^{11} \, \mathrm{M}_{\odot}$ hosting an AGN is high (80 per cent) at $z \ge 3$ and lower (≤ 50 per cent) at z < 3 (Fig. 9). While the time evolution is quite uncertain in observations due to the low number statistics at high redshift, this could be tested further in lower mass galaxies. Indeed, we find that the time evolution of the AGN fraction in the simulations is somewhat similar in lower mass galaxies with e.g. $M_{\star} \sim 10^{10} \, \mathrm{M}_{\odot}$ (Fig. 8). This work motivates the need to test this in observations, with multiwavelength surveys to measure the galaxies' properties and X-ray detections of AGN.

The fraction of low-mass galaxies of $M_{\star} \sim 10^9 \, \rm M_{\odot}$ hosting an AGN at low redshift can also vary from one simulation to another. This has important implications for BH formation and the ability of BHs to growth at early times. Comparing in detail the AGN fraction of these galaxies to the current systematic search of AGN in local dwarf galaxies (Reines, Greene & Geha 2013; Baldassare et al. 2015; Chilingarian et al. 2018; Mezcua et al. 2018; Greene et al. 2019; Birchall, Watson & Aird 2020) will bring us a new way of constraining the BH physics in cosmological simulations, particularly the seeding, but probably also AGN feedback. Recently, there has been evidence for AGN outflows in dwarf galaxies (Manzano-King, Canalizo & Sales 2019; Liu et al. 2020), and in simulations (Koudmani, Henden & Sijacki 2020). We will investigate the AGN/low-mass galaxy regime connection in detail in our future work.

7.3 AGN obscuration and AGN variability

The obscuration of the AGN is a key aspect when comparing simulated and observed populations of AGNs. It may be the key to explain some of the discrepancies that we found in this paper. Gas and dust content along the line of sight can limit or extinguish the radiation coming from the AGN (see Brandt & Alexander 2015, for a review). Obscuration and particularly the fraction of AGN that could be obscured have been an active field of research, but the picture is still unclear (e.g. Ueda et al. 2003, 2014; Merloni et al. 2014; Buchner et al. 2015; Georgakakis et al. 2017, and references therein). There is also evidence for obscuration at high redshifts (e.g. z > 4 Gilli et al. 2014; Vito et al. 2020), and even a possible large fraction of \sim 50 per cent obscured AGN in the range $z \sim$ 4–6 (Vito et al. 2018).

In this paper, we have used several obscuration models to make predictions for future observational surveys. Unsurprisingly, we found that obscuration can play a crucial role, and can lead to large uncertainties in the number of AGNs that will be detectable with the upcoming Athena mission and AXIS and LynX concept missions. Constraining the obscured fraction of AGN as a function of redshift, and BH/galaxy properties (e.g. BH and galaxy mass, AGN luminosity, galaxy compactness, sizes, and SFR), appears crucial for deriving more accurate predictions for these new missions. Given the discrepancies that we found through this paper with current AGN observations, addressing AGN obscuration in the near future is essential. On the simulation side, we could employ simulations

with higher resolution to link galaxies and their BHs to their column density (possibly with machine learning techniques). Such a model would give us the likely column density and obscuration level for a given BH in a given galaxy, a model easily applicable to post-processing analyses of large-scale cosmological simulations.

Finally, the uncertainty on AGN obscuration in observations can only result in a possible increase of the number of observed AGNs. Therefore, regimes in the simulations for which fewer AGNs are produced than in observations are likely robust and can already be used to improve next-generation simulations. This is mostly the case for bright AGN at low redshift in half of the simulations studied here, and more globally for the EAGLE simulation. This could be due to too efficient AGN feedback.

More analyses of the bright AGN regime are needed, especially as the high-luminosity end of the luminosity function is sensitive to time variability, as shown in this paper. The impact of AGN variability that we find e.g. on the AGN luminosity function could also be found for variations of the radiative efficiency, which is a constant parameter in all cosmological simulations.

8 CONCLUSIONS

In this paper, the second in our series, we have analysed the six Illustris, TNG100, TNG300, Horizon-AGN, EAGLE, and SIMBA large-scale cosmological simulations. We focused on the populations of AGNs produced by the simulations and how their properties evolve with both redshift and their BH/galaxies properties. Our goals were to understand how the simulations differ and to identify features in the AGN population that could help us to rule out and/or improve the subgrid physics modelling in simulations. Through this paper, we have addressed several comparisons between the simulated AGN populations and observational constraints. We have also predicted what population of BHs the next-generation X-ray missions Athena, AXIS, and LynX could detect, and how accessing the fainter AGN regime will help us to constrain further the physics of cosmological simulations. We summarize our main findings below.

- (i) The AGN populations produced by Illustris, TNG100, Horizon-AGN, EAGLE, and SIMBA are different on many aspects. These differences are caused by the various subgrid models of BH and galaxy formation physics.
- (ii) Some simulations show a strong decrease of the median BH bolometric luminosity in massive galaxies (Fig. 2), due to AGN feedback. The trend is not as strong in current observational constraints.
- (iii) The distribution of Eddington ratios moves towards lower $f_{\rm Edd}$ ratios with time, for all the simulations (Fig. 3). However, the simulations do not have the same shapes and peak at different ratios for different BH masses. At z=0, the simulations are in agreement with the observations of Heckman et al. (2004) for BHs of $M_{\rm BH} \leq 10^8\,{\rm M}_\odot$, but not for more massive BHs: Simulations either produce AGN with higher $f_{\rm Edd}$ (Illustris) or lower $f_{\rm Edd}$ distributions (TNG and SIMBA). A good agreement is found for Horizon-AGN.
- (iv) Considering all the AGNs ($L_{\rm bol} > 10^{43} \, {\rm erg \, s^{-1}}$) and independently of their BH masses, we find good agreement for the mean $f_{\rm Edd}$ with observations (Kelly & Shen 2013) at high redshift (z=4–3) for all the simulations. However, at z=0 we note that the simulations predict higher mean $f_{\rm Edd}$.
- (v) The simulations produce different AGN luminosity functions (bolometric and hard X-ray, Fig. 5); the discrepancies can be ≥1 dex at fixed luminosity. Compared to observations, most of the simulations produce too many AGNs of any luminosity at high

redshift, and the agreement improves towards lower redshift. We find the opposite behaviour for EAGLE, which agrees better with constraints at high redshift.

- (vi) Several simulations produce very few of the brightest AGN (Fig. 5). However, we found that the bright end of the luminosity function is sensitive to AGN short time-scale variability (Fig. 6), which is not resolved in the simulations.
- (vii) The simulations have AGN number densities peaking at different redshifts (Fig. 7). In observations, brighter AGNs peak at a higher redshift than fainter AGNs (Ueda et al. 2014; Aird et al. 2015; Buchner et al. 2015). In simulations, we find that only the TNG and SIMBA simulations clearly present the same trend, while peaking at different redshifts.
- (viii) Several simulations produce too many faint AGNs with $\log_{10} L_x/(\text{erg s}^{-1}) = 42-43$ [and $\log_{10} L_x/(\text{erg s}^{-1}) = 43-44$ for some of them] in low-mass galaxies of $M_{\star} = 10^9-10^{10} \, \text{M}_{\odot}$ with respect to observations (Fig. 7), especially at $z \ge 1$.
- (ix) All the simulations have a hard time producing a population of AGNs in good agreement with observational constraints at *both* high and low redshifts, but also for *both* faint and brighter AGNs (Fig. 7).
- (x) The fraction of galaxies, of a given mass, hosting an AGN varies from simulation to simulation, with the largest differences for galaxies of $M_{\star} \sim 10^9$ and $10^{11} \, \mathrm{M}_{\odot}$ (Fig. 8). The differences in the low-mass regime have important implications for the search of AGN in local dwarf galaxies (see the discussion in Section 7.1). For the massive galaxies, we find that the AGN fraction of all the simulations has the same trend as observations (high fraction at high redshifts, decreasing with time), but some simulations have a lower fraction at z < 2 due to strong AGN feedback.
- (xi) The lower fraction of AGN found in simulated massive galaxies with respect to observations at low redshift indicates that simulations all need AGN feedback that must be efficient enough to quench star formation, but somehow should not completely limit the AGN activity itself.

New constraints on the AGN population will come from the upcoming Athena X-ray mission and the concept missions AXIS and LynX. We showed that the population and properties of AGNs vary from one simulation to another, and that all individual simulations have a hard time producing AGN in agreement with current observations for all the luminosity and redshift regimes. However, our analysis of six large-scale cosmological simulations covers many different modellings, and thus is powerful to better estimate the uncertainties on the predicted AGN population to be detected by the new missions.

- (i) All the simulations studied here predict different total numbers of AGN detections as a function of redshift, sometimes varying by more than one order of magnitude (Fig. 11).
- (ii) The sensitivity of these missions will be more than one order of magnitude better than current X-ray facilities, and will allow us to observe fainter AGNs. We find that Athena, AXIS, and LynX will make it possible to observe and recover the intrinsic distribution of AGN luminosity (and the corresponding BH mass distribution) to different levels (Figs 12, 13, and 14). The shape of the AGN luminosity (and BH mass) distributions being different for all the simulations, the new missions will provide us with a crucial pathway to constrain simulation subgrid models.

In the next paper of our series, we will link the BHs to their host galaxies. Particularly, we will investigate in detail the connections between the simulated AGN populations and the star-forming properties of their host galaxies in large-scale cosmological simulations.

ACKNOWLEDGEMENTS

We thank Alexey Vikhlinin and Niel Brandt for very fruitful discussions on the next-generation X-ray missions. We thank the anonymous reviewer for valuable suggestions that helped improve the paper. JA acknowledges support from a UKRI Future Leaders Fellowship (grant code: MR/T020989/1). DAA acknowledges support by NSF grant AST-2009687 and by the Flatiron Institute, which is supported by the Simons Foundation. YRG acknowledges the support of 'Juan de la Cierva Incorporation' fellowship (IJC2019-041131-I). MV acknowledges support through NASA ATP grants 16-ATP16-0167, 19-ATP19-0019, 19-ATP19-0020, and 19-ATP19-0167, and NSF grants AST-1814053, AST-1814259, AST-1909831, and AST-2007355.

DATA AVAILABILITY

The data from the Illustris and the TNG100 simulations can be found on their respective websites https://www.illustris-project.org and ht tps://www.tng-project.org. The data from the EAGLE simulation can be obtained upon request to the EAGLE team at their website http://icc.dur.ac.uk/Eagle/. The data from the SIMBA simulation can be found on the website http://simba.roe.ac.uk/. Some catalogues of the Horizon-AGN simulation are available at https://www.horizon-simulation.org/data.html, and some others are available on request.

REFERENCES

Aird J., Nandra K., Georgakakis A., Laird E. S., Steidel C. C., Sharon C., 2008, MNRAS, 387, 883

Aird J. et al., 2010, MNRAS, 401, 2531

Aird J. et al., 2012, ApJ, 746, 90

Aird J. et al., 2013, ApJ, 775, 41

Aird J., Coil A. L., Georgakakis A., Nandra K., Barro G., Pérez-González P. G., 2015, MNRAS, 451, 1892

Aird J., Coil A. L., Georgakakis A., 2017, MNRAS, 465, 3390

Aird J., Coil A. L., Georgakakis A., 2018, MNRAS, 474, 1225

Ananna T. T. et al., 2019, ApJ, 871, 240

Ananna T. T. et al., 2020, ApJ, 903, 85

Anglés-Alcázar D., Özel F., Davé R., 2013, ApJ, 770, 5

Anglés-Alcázar D., Özel F., Davé R., Katz N., Kollmeier J. A., Oppenheimer B. D., 2015, ApJ, 800, 127

Anglés-Alcázar D., Davé R., Faucher-Giguère C.-A., Özel F., Hopkins P. F., 2017a, MNRAS, 464, 2840

Anglés-Alcázar D., Faucher-Giguère C.-A., Quataert E., Hopkins P. F., Feldmann R., Torrey P., Wetzel A., Kereš D., 2017b, MNRAS, 472, L109

Angles-Alcazar D. et al., 2020, ApJ, 917, 53

Baldassare V. F., Reines A. E., Gallo E., Greene J. E., 2015, ApJ, 809, L14

Baron D., Ménard B., 2019, MNRAS, 487, 3404

Birchall K. L., Watson M. G., Aird J., 2020, MNRAS, 492, 2268

Bondi H., Hoyle F., 1944, MNRAS, 104, 273

Brandt W. N., Alexander D. M., 2015, A&AR, 23, 1

Brusa M. et al., 2009, ApJ, 693, 8

Buchner J., Bauer F. E., 2017, MNRAS, 465, 4348

Buchner J. et al., 2015, ApJ, 802, 89

Carraro R. et al., 2020, A&A, 642, A65

Chilingarian I. V., Katkov I. Y., Zolotukhin I. Y., Grishin K. A., Beletsky Y., Boutsia K., Osip D. J., 2018, ApJ, 863, 1

Churazov E., Sazonov S., Sunyaev R., Forman W., Jones C., Böhringer H., 2005, MNRAS, 363, L91

Civano F. et al., 2011, ApJ, 741, 91

```
Civano F. et al., 2016, ApJ, 819, 62
```

Cowley M. J. et al., 2016, MNRAS, 457, 629

Crain R. A. et al., 2015, MNRAS, 450, 1937

Davé R., Anglés-Alcázar D., Narayanan D., Li Q., Rafieferantsoa M. H., Appleby S., 2019, MNRAS, 486, 2827

DeGraf C., Dekel A., Gabor J., Bournaud F., 2017, MNRAS, 466, 1462

Donnari M. et al., 2019, MNRAS, 485, 4817

Donnari M. et al., 2021, MNRAS, 500, 4004

Donnari M., Pillepich A., Nelson D., Marinacci F., Vogelsberger M., Hernquist L., 2020, MNRAS, 506, 4760

Dubois Y. et al., 2014, MNRAS, 444, 1453

Dubois Y., Peirani S., Pichon C., Devriendt J., Gavazzi R., Welker C., Volonteri M., 2016, MNRAS, 463, 3948

Duras F. et al., 2020, A&A, 636, A73

Fornasini F. M., Civano F., Fabbiano G., Elvis M., Marchesi S., Miyaji T., Zezas A., 2018, ApJ, 865, 43

Gabor J. M., Bournaud F., 2014, MNRAS, 441, 1615

Genel S. et al., 2014, MNRAS, 445, 175

Georgakakis A. et al., 2015, MNRAS, 453, 1946

Georgakakis A. et al., 2017, MNRAS, 469, 3232

Georgantopoulos I., Akylas A., 2010, A&A, 509, A38

Giallongo E. et al., 2015, A&A, 578, A83

Gilli R., Comastri A., Vignali C., Hasinger G., 2007, Prog. Theor. Phys. Suppl., 169, 286

Gilli R., Comastri A., Hasinger G., 2007, A&A, 463, 79

Gilli R. et al., 2011, ApJ, 730, L28

Gilli R. et al., 2014, A&A, 562, A67

Goulding A. D., Alexander D. M., Lehmer B. D., Mullaney J. R., 2010, MNRAS, 406, 597

Greene J. E., Strader J., Ho L. C., 2019, ARA&A, 58, 257

Gültekin K. et al., 2009, ApJ, 698, 198

Habouzit M., Volonteri M., Dubois Y., 2017, MNRAS, 468, 3935

Habouzit M. et al., 2019, MNRAS, 484, 4413

Habouzit M. et al., 2020, MNRAS, 503, 1940

Häring N., Rix H.-W., 2004, ApJ, 604, L89

Heckman T. M., Kauffmann G., Brinchmann J., Charlot S., Tremonti C., White S. D. M., 2004, ApJ, 613, 109

Hirschmann M., Dolag K., Saro A., Bachmann L., Borgani S., Burkert A., 2014, MNRAS, 442, 2304

Hopkins P. F., Quataert E., 2011, MNRAS, 415, 1027

Hopkins P. F., Richards G. T., Hernquist L., 2007, ApJ, 654, 731

Kauffmann G. et al., 2003, MNRAS, 346, 1055

Kaviraj S., Martin G., Silk J., 2019, MNRAS, 489, L12

Kelly B. C., Shen Y., 2013, ApJ, 764, 45

Kelly B. C., Vestergaard M., Fan X., Hopkins P., Hernquist L., Siemiginowska A., 2010, ApJ, 719, 1315

Kollmeier J. A. et al., 2006, ApJ, 648, 128

Koudmani S., Henden N. A., Sijacki D., 2020, MNRAS, 503, 3568

Koulouridis E. et al., 2018, AAP, 620, A4

Kriek M. et al., 2007, ApJ, 669, 776

La Franca F. et al., 2005, ApJ, 635, 864

Lehmer B. D. et al., 2019, ApJS, 243, 3

Li Y. et al., 2019, ApJ, 895, 102

Liu W., Veilleux S., Canalizo G., Rupke D. S. N., Manzano-King C. M., Bohn T. U V., 2020, ApJ, 905, 166

Lusso E. et al., 2012, MNRAS, 425, 623

McAlpine S. et al., 2016, Astron. Comput., 15, 72

McAlpine S., Bower R. G., Harrison C. M., Crain R. A., Schaller M., Schaye J., Theuns T., 2017, MNRAS, 468, 3395

McAlpine S., Bower R. G., Rosario D. J., Crain R. A., Schaye J., Theuns T., 2018, MNRAS, 481, 3118

Magorrian J. et al., 1998, AJ, 115, 2285

Man Z.-y., Peng Y.-j., Kong X., Guo K.-x., Zhang C.-p., Dou J., 2019, MNRAS, 488, 89

Manzano-King C. M., Canalizo G., Sales L. V., 2019, ApJ, 884, 54

Marchesi S. et al., 2016, ApJ, 827, 150

Marchesi S. et al., 2020, A&A, 642, A184

Marsan Z. C., Marchesini D., Brammer G. B., Geier S., Kado-Fong E., Labbé I., Muzzin A., Stefanon M., 2017, ApJ, 842, 21

Mendez A. J. et al., 2013, ApJ, 770, 40

Merloni A. et al., 2014, MNRAS, 437, 3550

Mezcua M., Civano F., Marchesi S., Suh H., Fabbiano G., Volonteri M., 2018, MNRAS, 478, 2576

Miyaji T. et al., 2015, ApJ, 804, 104

Mullaney J. R. et al., 2012, ApJ, 753, L30

Mushotzky R., 2018, in Herder J.-W. A. d., Nikzad S., Nakazawa K., eds, Proc. SPIE Conf. Ser. Vol. 10699, Space Telescopes and Instrumentation 2018: Ultraviolet to Gamma Ray. SPIE, Bellingham, p. 1069929

Mushotzky R. et al., 2019, Bull. Am. Astron. Soc., 51, 107

Nandra K. et al., 2013, preprint (arXiv:1306.2307)

Negri A., Volonteri M., 2017, MNRAS, 467, 3475

Nelson D. et al., 2018, MNRAS, 475, 624

Novak G. S., Ostriker J. P., Ciotti L., 2011, ApJ, 737, 26

Peirani S. et al., 2017, MNRAS, 472, 2153

Pillepich A. et al., 2018, MNRAS, 473, 4077

Ramos Almeida C., Ricci C., 2017, Nat. Astron., 1, 679

Reines A. E., Greene J. E., Geha M., 2013, ApJ, 775, 116

Ricci C. et al., 2017, Nature, 549, 488

Ricci F., Marchesi S., Shankar F., La Franca F., Civano F., 2017, MNRAS, 465, 1915

Rosas-Guevara Y. M. et al., 2015, MNRAS, 454, 1038

Rosas-Guevara Y., Bower R. G., Schaye J., McAlpine S., Dalla Vecchia C., Frenk C. S., Schaller M., Theuns T., 2016, MNRAS, 462, 190

Russell H. R., McNamara B. R., Edge A. C., Hogan M. T., Main R. A., Vantyghem A. N., 2013, MNRAS, 432, 530

Schaye J. et al., 2015, MNRAS, 446, 521

Schirra A. P. et al., 2021, MNRAS, 508, 4816

Schulze A., Wisotzki L., 2010, A&A, 516, A87

Schulze A. et al., 2015, MNRAS, 447, 2085

Shen Y., Kelly B. C., 2012, ApJ, 746, 169

Sijacki D., Vogelsberger M., Genel S., Springel V., Torrey P., Snyder G. F., Nelson D., Hernquist L., 2015, MNRAS, 452, 575

Silk J., Mamon G. A., 2012, Res. Astron. Astrophys., 12, 917

Snaith O. N., Park C., Kim J., Rosdahl J., 2018, MNRAS, 477, 983

Somerville R. S., Davé R., 2015, ARA&A, 53, 51

Terrazas B. A. et al., 2019, MNRAS, 493, 1888

The Lynx Team, 2018, preprint (arXiv:1809.09642)

Thomas N., Davé R., Anglés-Alcázar D., Jarvis M., 2019, MNRAS, 487, 5764

Thomas N., Dave R., Jarvis M. J., Angles-Alcazar D., 2020, MNRAS, 503, 3492

Ueda Y., Akiyama M., Ohta K., Miyaji T., 2003, ApJ, 598, 886

Ueda Y., Akiyama M., Hasinger G., Miyaji T., Watson M. G., 2014, ApJ, 786, 104

Vito F., Gilli R., Vignali C., Comastri A., Brusa M., Cappelluti N., Iwasawa K., 2014, MNRAS, 445, 3557

Vito F. et al., 2016, MNRAS, 463, 348

Vito F. et al., 2018, MNRAS, 473, 2378

Vito F. et al., 2020, A&A, 642, A149

Vogelsberger M., Genel S., Sijacki D., Torrey P., Springel V., Hernquist L., 2013, MNRAS, 436, 3031

Vogelsberger M. et al., 2014a, Nature, 509, 177

Vogelsberger M. et al., 2014b, MNRAS, 444, 1518

Vogelsberger M., Marinacci F., Torrey P., Puchwein E., 2020, Nat. Rev. Phys., 2, 42

Volonteri M., Dubois Y., Pichon C., Devriendt J., 2016, MNRAS, 460,

Weinberger R. et al., 2017, MNRAS, 465, 3291

Weinberger R. et al., 2018, MNRAS, 479, 4056

Xue Y. Q. et al., 2010, ApJ, 720, 368

APPENDIX A: IMPACT OF PARAMETERS/MODELS ON THE AGN LUMINOSITY FUNCTION

In this paper, we discussed the AGN luminosity function for the Illustris, TNG100, TNG300, Horizon-AGN, EAGLE, and SIMBA simulations. In the main text of the paper, we choose a given set of parameters/models:

- (i) We choose the radiative efficiency that was used in the different simulations to compute AGN luminosity, i.e. $\epsilon_{\rm r}=0.2$ for Illustris, TNG100, and TNG300, and $\epsilon_{\rm r}=0.1$ for Horizon-AGN, EAGLE, and SIMBA. In practice, varying $\epsilon_{\rm r}=0.2$ in our post-processing analysis simply shifts the AGN luminosity to fainter or brighter luminosity.
- (ii) To compute AGN luminosity, we considered AGN radiatively efficient if $f_{\rm Edd} > 0.1$ and radiatively inefficient otherwise. A fraction of the AGNs are fainter than when assuming that all AGNs are radiatively efficient. This mostly affects the faint end of the AGN distribution.
- (iii) To compute the X-ray luminosity of the AGN, we use the BC of Hopkins et al. (2007).
- (iv) Finally, we did not correct for AGN variability, which cannot be captured in the simulations, in most of the paper. We showed the possible impact of AGN variability in Fig. 6.

Here, we investigate the impact of these parameters.

A1 Impact of the model to compute AGN luminosity on the AGN luminosity function

Often used in the analysis of cosmological simulations, the assumption that all AGNs are radiatively efficient can increase significantly the number of AGNs in certain luminosity bins. In Fig. A1 (top panels), we show the hard X-ray (2–10 keV) AGN luminosity functions when making this assumption. Compared to our previous model to compute the AGN luminosities, the main consequence is an increase of the number of AGNs for luminosities of $L_{\rm x} \le 10^{44}~{\rm erg~s^{-1}}$ and of $L_{\rm bol} \le 10^{45}~{\rm erg~s^{-1}}$ at all redshifts.

In Fig. A1 (bottom panels), we show the impact of the BC on the hard X-ray luminosity function, and use the correction of Duras et al. (2020) instead of Hopkins et al. (2007). The main effect is a shift in the luminosity function of all simulations towards more luminous AGN. The choice of the BC does not affect the conclusions of the paper.

A2 Impact of the model to compute AGN luminosity on the AGN fraction in massive galaxies

We show in Fig. A2 the same figure as Fig. 9 but using the same radiative efficiency of $\epsilon_r = 0.1$ for all the simulations (instead of $\epsilon_r = 0.2$ for the Illustris and TNG simulations) and we assume that all the simulated AGNs are radiatively efficient. This means that AGNs with

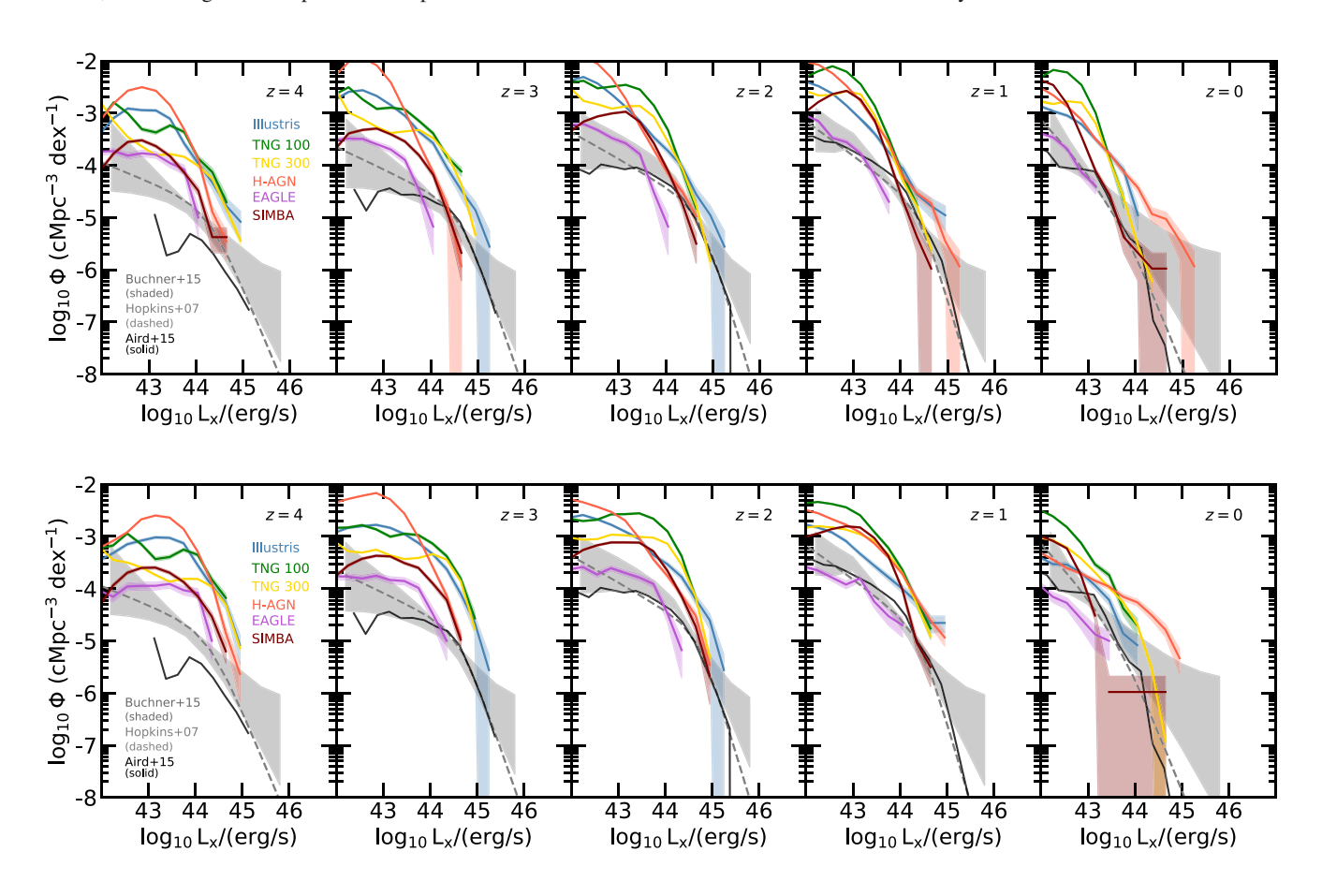


Figure A1. Top panels: Hard X-ray (2–10 keV) AGN luminosity function for Illustris, TNG100, TNG300, Horizon-AGN, EAGLE, and SIMBA. Observational constraints from Hopkins et al. (2007), Buchner et al. (2015), and Aird et al. (2015) and are shown in grey. Here, we assume that all BHs are radiatively efficient AGN. Compared to the results presented in Fig. 5, this assumption increases the number of AGNs, particularly in the faint end of the luminosity function, i.e. for $\log_{10} L_x/(\text{erg s}^{-1}) \le 44$. Bottom panels: Same as Fig. 5 but with the BC of Duras et al. (2020) instead of Hopkins et al. (2007). The luminosity functions slightly shift towards more luminous AGN.

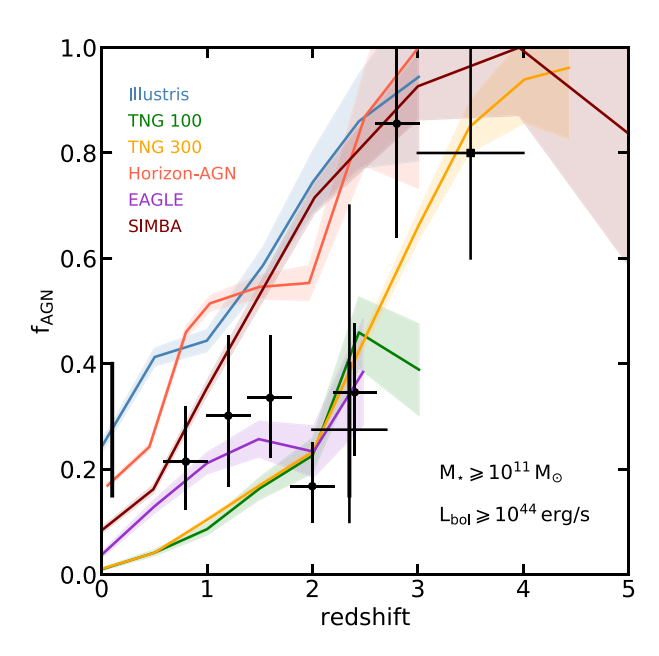


Figure A2. Fraction of AGN with $L_{\rm bol} \geqslant 10^{44}~{\rm erg~s^{-1}}$ in massive galaxies of $M_{\star} \geqslant 10^{11}~{\rm M}_{\odot}$ (right-hand panels). Same as Fig. 9, but assuming $\epsilon_{\rm r} = 0.1$ for all the simulations and that all AGNs are radiatively efficient when computing their luminosities. The number of AGNs in Illustris and TNG is reduced slightly when using $\epsilon_{\rm r} = 0.1$, but the dominant effect is an enhancement of the fractions of AGN in all the simulations when we assume that all AGNs are radiatively efficient.

 $f_{\rm Edd} \leq 0.1$ are not considered as radiatively inefficient, and therefore now have higher luminosity. Consequently, we find higher fractions of AGN for in all the simulations. This particularly affects the AGN fraction at $z \leq 2.5$ in these massive galaxies (see also Habouzit et al. 2019).

APPENDIX B: PREDICTIONS FOR NEW X-RAY MISSIONS

B1 Detection limits

We convert the 0.5–2 keV sensitivity curves shown in Fig. 10 to the 2–10 keV band for each of the surveys by applying the following K-correction and assuming $\gamma = 1.4$:

$$F_{2-10\,\text{keV}} = F_{0.5-2\,\text{keV}} \, \frac{10^{2-\gamma} - 2^{2-\gamma}}{2^{2-\gamma} - 0.5^{2-\gamma}} \, (1+z)^{\gamma-2}. \tag{B1}$$

The sensitivity limit to detect a source depends on the area of sky covered by the surveys and exposure time. We derive a fixed flux sensitivity for each survey, i.e. that we do not vary the sensitivity across the survey field of view. In practice, the sensitivity is higher at the edges of the single pointing's field of view, which can be improved by overlapping the pointings. Here, we do not enter in such detail to compute the detection limit since the Athena, Axis, and LynX surveys are not yet finalized. We express the flux limits as 2–10 keV X-ray luminosity limits with the expression $L_{\rm detection} = 4\pi D_{\rm L}^2 \times F_{\rm detection}$, with $D_{\rm L}^2$ the luminosity distance. The luminosity distance depends on redshift and cosmology; we employ the cosmology of each of the simulations, respectively. As an example, we show the 2–10 keV luminosity limits to detect an AGN in Illustris (similar limits are found for the other simulations), in Fig. B1.

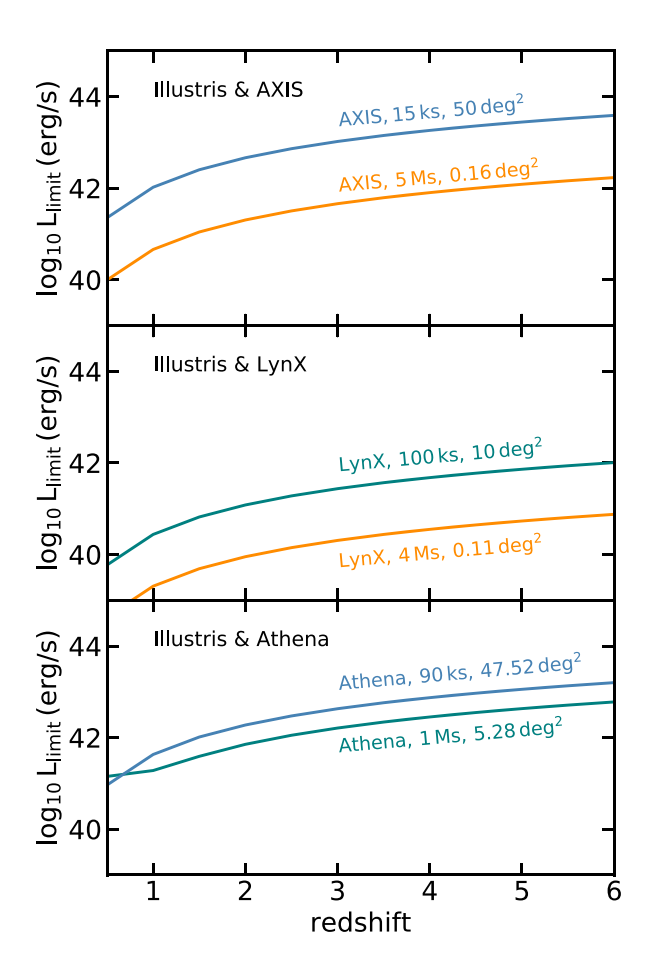


Figure B1. Hard (2–10 keV) X-ray luminosity limits to detect an AGN with possible Athena, AXIS, and LynX surveys. We derive these limits from the sensitivity curve, exposure time, and size of the mission surveys.

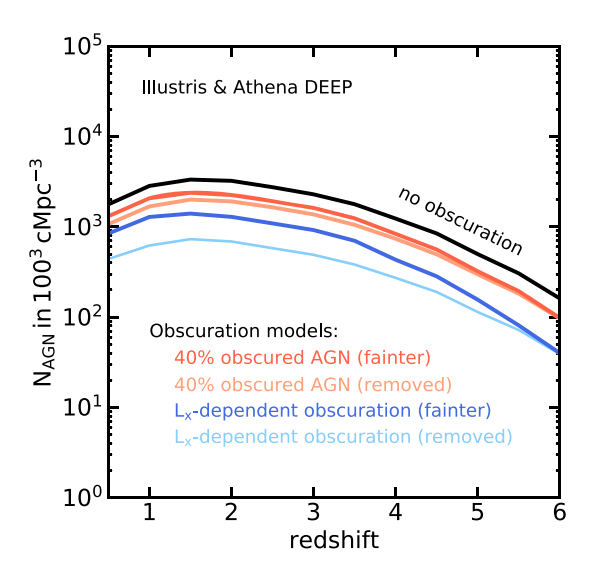


Figure B2. Effect of our AGN obscuration models on the total number of detectable AGNs in 100^3 cMpc 3 , for the Illustris simulation and the Athena DEEP survey. A similar effect is found for the other simulations and surveys. The first models assume that 40 per cent of the AGNs are heavily obscured, and the two other models assume an anticorrelation between the fraction of obscured AGNs and their luminosity. We either remove the obscured AGN from the samples (*removed*) or decrease their luminosity (*fainter*).

Table B1. Best-fitting equations for the number of AGNs [per $(100 \, \text{cMpc})^3$] observable with the upcoming Athena mission and NASA concept missions AXIS and LynX. We use the possible surveys described in Table 1, and our second model for obscuration depending on both redshift and AGN X-ray $(2-10 \, \text{keV})$ luminosity: Obscured AGNs are either removed (*removed* model) or detected as fainter AGN (*faint* model). The two models represent the upper and lower edges of the shaded regions in Fig. 11. The equations follow: $N_{\text{AGN}}(z)/(100 \, \text{cMpc})^3 = ax + bx^2 + cx^3 + dx^4 + ex^5 + f$. We provide the fits for all the simulations in the 1–5th rows. We also add the mean AGN detections over all the simulations $\bar{N}_{\text{AGN}}(z)$ in the sixth row, and a region enclosing all the simulations can be defined by $(1/8-2) \times \bar{N}_{\text{AGN}}$.

Simulations	Missions	Coefficients (a, b, c, d, e, f) Obsc. z -, L_x -dependent model (removed)	Coefficients (a, b, c, d, e, f) Obsc. z -, L_x -dependent model (faint)
Illustris	Athena DEEP Athena WIDE AXIS DEEP AXIS WIDE LynX DEEP LynX WIDE	(1062.6, -540.7, 102.6, -8.5, 0.3, 25.9) (98.0, -48.3, -6.7, 3.0, -0.2, 455.5) (451.6, -66.7, -74.3, 20.4, -1.5, 617.2) (-438.4, 578.7, -255.5, 43.4, -2.5, 662.1) (1344.0, -848.9, 157.1, -9.7, 0.0, 1014.9) (656.0, -199.0, -43.1, 17.2, -1.3, 633.5)	(2489.9, -1425.4, 331.4, -37.5, 1.7, -80.7) (-1293.7, 904.1, -321.5, 50.8, -2.9, 1493.3) (957.2, -258.1, -105.0, 33.0, -2.4, 1950.6) (-2526.6, 2251.9, -822.4, 126.8, -7.0, 2070.9) (4352.2, -1788.0, -10.5, 63.3, -5.7, 3260.7) (1390.1, -261.3, -195.9, 55.8, -4.0, 2093.5)
TNG100	Athena DEEP Athena WIDE AXIS DEEP AXIS WIDE LynX DEEP LynX WIDE	(1679.4, -1675.9, 522.9, -70.8, 3.6, 1298.1) (-489.5, -162.6, 53.7, -2.9, -0.2, 2138.0) (818.4, -1013.9, 295.7, -36.3, 1.7, 1930.7) (-182.6, -296.1, 82.6, -7.0, 0.1, 2096.6) (569.6, -811.9, 216.4, -23.0, 0.9, 2234.6) (691.1, -888.8, 248.4, -28.9, 1.2, 2019.2)	(9655.1, -7707.3, 2302.1, -306.7, 15.3, 557.1) (-7123.9, 4064.8, -1317.0, 207.8, -12.3, 7279.0) (1505.7, -3208.2, 984.1, -118.2, 5.0, 8134.5) (-8160.3, 5413.5, -1942.2, 320.6, -19.3, 8504.9) (6421.4, -6216.0, 1766.8, -219.5, 10.3, 7954.3) (4075.4, -5140.0, 1589.7, -205.9, 9.8, 7677.8)
Horizon-AGN	Athena DEEP Athena WIDE AXIS DEEP AXIS WIDE LynX DEEP LynX WIDE	(4611.1, -2967.2, 951.7, -159.0, 10.5, -1274.2) (3322.2, -2431.7, 829.0, -138.9, 9.0, -701.3) (2780.3, -979.6, 121.2, -14.4, 1.5, -224.2) (1622.1, -594.8, 157.5, -39.1, 3.7, -125.8) (2929.7, -192.5, -467.6, 118.4, -8.2, 318.6) (2902.1, -854.9, 16.4, 8.7, 0.1, -190.4)	(14 974.7, -10 892.3, 3568.2, -558.7, 33.6, -4536.0) (6250.7, -5155.7, 1833.6, -303.8, 19.0, -1140.4) (15 381.7, -9970.1, 3146.2, -519.2, 34.2, -3280.4) (6266.8, -4489.1, 1632.4, -300.5, 21.0, -1074.5) (13 390.5, -1884.4, -1193.1, 297.5, -17.8, -293.6) (16 153.3, -9860.2, 3065.4, -522.3, 35.9, -3185.2)
EAGLE	Athena DEEP Athena WIDE AXIS DEEP AXIS WIDE LynX DEEP LynX WIDE	(129.2, -113.5, 36.3, -5.2, 0.3, 68.1) (-154.2, 83.3, -24.5, 3.5, -0.2, 181) (-114.9, 20.7, -1.7, 0.1, -0.0, 283.5) (-191.5, 124.9, -41.0, 6.3, -0.4, 206.9) (120.4, -273.0, 110.5, -17.9, 1.0, 443.9) (-28.6, -54.5, 24.4, -3.9, 0.2, 273.9)	(403.4, -328.7, 102.2, -14.2, 0.7, 60.1) (-438.5, 240.8, -69.0, 9.7, -0.5, 407.5) (-567.5, 263.1, -73.5, 10.6, -0.6, 807.6) (-530.1, 350.5, -113.0, 17.0, -1.0, 475.2) (-85.4, -418.8, 179.0, -28.1, 1.5, 1518.9) (-799.9, 438.4, -137.8, 21.4, -1.3, 994.1)
SIMBA	Athena DEEP Athena WIDE AXIS DEEP AXIS WIDE LynX DEEP LynX WIDE	(145.8, -429.9, 171.9, -27.2, 1.5, 740.3) (-502.4, 14.9, 35.0, -7.5, 0.5, 1013.1) (-714.9, 130.3, 3.9, -3.7, 0.3, 1249.3) (-594.5, 105.8, 1.7, -2.5, 0.2, 1077.9) (-899.6, 225.4, -20.4, -0.7, 0.2, 1402.6) (-802.7, 183.8, -11.5, -1.6,0.2, 1307.5)	(5441.9, -5390.3, 1982.3, -320.4, 19.2, 157.1) (-1411.7, -205.3, 260.5, -56.3, 3.8, 2783.0) (-1107.6, -681.6, 378.9, -64.9, 3.8, 4020.2) (-1672.3, 187.5, 51.7, -14.0, 0.9, 3152.5) (-2532.4, 92.9, 170.3, -38.8, 2.6, 5423.8) (-1298.1, -574.1, 344.7, -59.9, 3.5, 4295.7)
Mean over all simulations	Athena DEEP Athena WIDE AXIS DEEP AXIS WIDE LynX DEEP LynX WIDE	(312.8, -14.5, -68.8, 16.3, -1.0, 549.2) (-404.9, 320.6, -143.8, 25.7, -1.6, 882.1) (-700.9, 852.2, -381.0, 64.8, -3.8, 1191.4) (-917.4, 851.4, -328.6, 51.6, -2.8, 1089.3) (-910.4, -1202.9, -564.3, 99.4, -6.0, 1616.2) (-762.6, 961.2, -432.6, 73.9, -4.3, 1259.5)	(3336.0, -2040.7, 459.4, -45.6, 1.7, 238.0) (-2162.3, 1337.9, -469.8, 76.4, -4.5, 2569.4) (-1413.5, 1598.9, -785.8, 141.6, -8.6, 3773.3) (-3462.0, 2744.2, -999.5, 157.3, -8.9, 3297.2) (-3344.1, 4889.9, -2290.4, 397.5, -23.4, 5967.8) (-1372.4, 1857.0, -924.9, 164.5, -9.8, 4017.5)

B2 Impact of obscuration models

Our predictions on the number of AGNs to be detected by X-ray missions are impacted by the number of AGNs that could be obscured. As the fraction of obscured AGNs is still uncertain, we test in Fig. B2 several obscuration models. We show our AGN luminosity- and redshift-dependent model, when we either remove the obscured AGNs (light blue line) or decrease their luminosity (dark blue line). We also test an obscuration model with 40 per cent of obscured AGN (independently of redshift, and AGN luminosity), shown as red and orange lines. The 40 per cent obscuration model leads to a higher number of detectable AGNs compared to our second AGN luminosity- and redshift-dependent obscuration models shown in Fig. B2.

B3 Best fits for the number of detectable AGN detectable

In Table B1, we provide the best-fitting equations for the number of AGNs [per $(100\,\mathrm{cMpc})^3$] observable with the upcoming Athena mission and NASA concept missions AXIS and LynX, for all the simulations (first to fifth rows). These predictions are shown in Fig. 11 (top panels). In the last row, we also provide the mean number of AGNs per $(100\,\mathrm{cMpc})^3$ over all the simulations $\bar{N}_{\mathrm{AGN}}(z)$. Using $(1/8-2)\times\bar{N}_{\mathrm{AGN}}$ allows us to enclose all the simulations.

This paper has been typeset from a $T_EX/ ext{LMT}_EX$ file prepared by the author.